Acta Cryst. (1993). A**49**, 624–642

Instrumental Effects on Measurements of Surface X-ray Diffraction Rods: Resolution Function and Active Sample Area

BY MICHAEL F. TONEY

IBM Almaden Research Center, IBM Research Division, San Jose, CA 95120, *USA*

AND DAVID G. WIESLER

National Institute of Standards and Technology, Gaithersburg, MD 20899, *USA*

(*Received* 6 *July* 1992; *accepted* 11 *January* 1993)

Abstract

This paper describes the effect of instrumental resolution on the line shapes and intensities of surface diffraction rods when the component of the scattering vector perpendicular to the surface (Q_z) is not small. Using a square-wave shape for the resolution function perpendicular to the scattering plane but an arbitrary in-plane shape, it is calculated how the resolution affects line shapes when the scattering vector is scanned parallel to the surface ($Q_{\|}$ scans). The approach used is to measure the line shape in $Q_{\|}$ scans at small Q_z and from this to determine how the $Q_{\|}$ line shapes depend on Q_z. Line shapes calculated in this manner are compared with data from an Ag(111) surface with excellent agreement, confirming the treatment. A similar approach is used to calculate the resolution correction that is needed to convert the measured diffraction-rod intensities into structure factors. Measurements of both peak intensity and integrated intensities in rocking scans are treated and the results are compared with those of previous treatments. Finally, the active sample area for an incident beam that is spatially nonuniform is calculated, as appropriate for experiments using focusing optics and wide incident slits. This approach accounts for the active area more accurately than the usual calculation assuming a uniform rectangular beam. The results described in this paper permit a better understanding of the effects of instrumental resolution on the line shapes of surface diffraction rods, enable more accurate determination of structure factors along these rods and are valid for nearly all Q_z.

I. Introduction

X-ray diffraction has long been recognized as the most powerful technique for structure determination of three-dimensional (3D) matter and in the past decade has been increasingly applied to the study of two-dimensional (2D) adsorbed layers and surfaces (Marra, Eisenberger & Cho, 1979; Feidenhans'l, 1989; Robinson, 1991; Toney & Melroy, 1991). The diffraction from a 2D crystal or the surface of a 3D crystal is characterized by rods of intensity, so named because they are sharp in the directions parallel to the surface yet are extended normal to the surface. Measurements of the intensity profiles along these surface diffraction rods provide a wealth of important information on the atomic structures of surfaces, interfaces and adsorbed layers (Robinson, 1986; Feidenhans'l, Pedersen, Nielsen, Grey & Johnson, 1986; Toney *et al.*, 1990; Toney, Gordon *et al.*, 1992; Gibbs, Ocko, Zehner & Mochrie, 1988; Sandy, Mochrie, Zehner, Huang & Gibbs, 1991). Thus, it is imperative to understand the instrumental effects that influence these intensities.

For 2D systems, the determination and interpretation of structure factors from the measured intensities is well understood for 'in-plane' measurements, *i.e.* those where Q_z, the component of the scattering vector perpendicular to the surface, is nearly zero (Robinson, 1991; Feidenhans'l, 1989; Robinson, 1988). Likewise, at sufficiently large Q_z ($\gtrsim 1$ Å^{-1}), structure factors can be accurately determined from the intensities measured along surface diffraction rods (Gibbs, Ocko, Zehner & Mochrie, 1988; Ocko, Gibbs, Huang, Zehner & Mochrie, 1991; Sandy, Mochrie, Zehner, Huang & Gibbs, 1991). However, for intermediate Q_z ($\sim$0.2–1 Å^{-1}), the connection between intensities and structure factors is complicated by rapidly varying instrumental effects caused by resolution volume anisotropy and partial illumination of the sample surface (and viewing by the detector). This paper bridges this 'Q_z' gap and provides a better understanding of these instrumental effects.

Here, we treat the symmetric four-circle diffraction geometry. We first consider a generalized instrumental resolution function, which consists of both spatial and angular variables and is necessary for the spatially nonuniform beam that we treat. We discuss conditions where the angular and spatial parts of this function decouple into the usual resolution function (dependent only on angular variables) and a more

ISSN 0108-7673 © 1993

general form for the active-area function. These conditions are reasonably common, which provides good justification for the decoupling and the widespread use of the usual resolution function. We specify the resolution function with a square-wave shape out of the scattering plane, but an arbitrary in-plane shape, and consider how this resolution function influences the measured intensities for specific scans used in surface X-ray scattering. We treat scans where the component of the scattering vector parallel to the surface ($Q_\parallel$) is varied but Q_z is constant ($Q_\parallel$ scans) and develop an expression to calculate the dependence of the $Q_\parallel$ line shape on Q_z. Next, we determine how the resolution affects the intensity of surface diffraction rods in Q_z scans and in rocking scans (integrated intensities). These permit an accurate determination of structure factors from the measured intensities for essentially all Q_z. Our results are then compared with previous treatments (Robinson, 1988; Altman, Estrup & Robinson, 1988; Gibbs, Ocko, Zehner & Mochrie, 1988; Ocko, Gibbs, Huang, Zehner & Mochrie, 1991; Sandy, Mochrie, Zehner, Huang & Gibbs, 1991). Following this, we derive an expression for the active sample area when the incident-beam profile is spatially nonuniform. Last, we compare our results with data from an Ag(111) surface and find excellent agreement, which supports our approach. In our treatment, we assume for simplicity that the surface scattering can be approximately separated into functions of $Q_\parallel$ and Q_z. Although this limits our results for $Q_\parallel$ scans, our results for integrated intensities are applicable even if this assumption is not completely fulfilled.

The results obtained in this paper show that by simply measuring the line shape in $Q_\parallel$ scans at small Q_z, one can accurately predict how the $Q_\parallel$ line shape depends on Q_z and how the resolution affects the intensity of surface diffraction rods. This is a major advantage, because it is not necessary to know the details of the resolution function to account for its effects; furthermore, our approach applies for arbitrary $Q_\parallel$ line shapes measured at small Q_z and is valid for essentially all Q_z. Thus, our results enable an accurate determination of structure factors for surface diffraction rods at moderate Q_z. Such measurements are important in certain 2D systems where the scattering intensity does not extend to large Q_z [*e.g.* self-assembled monolayers (Samant, Brown & Gordon, 1991) and interfacial alloys in metal multilayers (Rabedeau, Toney, Harp, Farrow & Marks, 1992; Toney, Farrow, Marks, Harp & Rabedeau, 1992)].

Before beginning the body of this paper, it is useful to review some of the features of surface diffraction. The surface diffraction rods are labeled by the discrete indices *hk*, which refer to the in-plane component of the reciprocal-lattice vectors, and by the continuous index Q_z (Feidenhans'l, 1989; Robinson, 1991; Toney & Melroy, 1991). The diffraction rods from a 2D crystal are termed Bragg rods. If the 2D crystal is a flat monolayer, then its structure factor is a monotonic slowly decreasing function of Q_z; the decrease arises from the Debye–Waller and atomic form factors. If the 2D crystal has vertical modulations or consists of more than one layer, the Bragg rod intensity will be modulated. The rods of scattered intensity from 3D crystal surfaces or interfaces are termed crystal truncation rods (CTRs) (Robinson, 1986) and the intensity profiles along these vary by several orders of magnitude. Near the bulk Bragg points, they are intense and depend strongly on Q_z but, halfway between Bragg points, the CTR intensity is comparable to that from a monolayer and is not strongly dependent on Q_z.

II. Instrumental resolution in surface X-ray scattering

A. Instrumental geometry

Here we briefly describe the symmetric four-circle ($\omega = 0$) diffraction geometry shown in Fig. 1(*a*). Detailed descriptions are found elsewhere (Busing & Levy, 1967; Robinson, 1989; Robinson, 1991; Toney & Melroy, 1991). In this geometry, the diffractometer operates so that $\omega \equiv \theta - (2\theta)/2 = 0$, where θ is the sample angle and 2θ is the scattering angle. The polar angle χ is the tilt of the sample within the plane bisecting the incoming and diffracted X-rays, *i.e.* it is the angle between the sample normal and the normal to the scattering plane. The relationship between χ and the incidence and exit angles of the X-rays relative to the sample surface, α and β, is $\sin\alpha = \sin\beta = \sin\chi\sin\theta$. In this geometry, α and β are equal and, when they are zero, the sample face is parallel to the scattering plane.

For surface X-ray scattering, it is convenient to resolve the scattering vector $\mathbf{Q}$ into components perpendicular and parallel to the surface, $Q_z\hat{\mathbf{z}}$ and $\mathbf{Q}_\parallel = Q_x\hat{\mathbf{x}} + Q_y\hat{\mathbf{y}}$, respectively, where $\hat{\mathbf{z}}$ is the surface normal and $\hat{\mathbf{x}}$ and $\hat{\mathbf{y}}$ are unit vectors parallel to the surface. These scattering-vector components are related to the diffractometer angles by

$$Q = (Q_\parallel^2 + Q_z^2)^{1/2} = (4\pi/\lambda)\sin\theta$$
$$Q_z = (4\pi/\lambda)\sin\alpha = Q\sin\chi, \qquad (1)$$

where λ is the X-ray wavelength. A second coordinate system is given by $\hat{\mathbf{s}}$, $\hat{\mathbf{t}}$ and $\hat{\mathbf{p}}$, where $\hat{\mathbf{s}}$ is parallel to $\mathbf{Q}$, $\hat{\mathbf{t}}$ is perpendicular to $\mathbf{Q}$ but in the scattering plane and $\hat{\mathbf{p}}$ is perpendicular to the scattering plane. The connection between this coordinate system and the sample coordinate system is illustrated in Fig. 1 and is given in Appendix *A*.

B. Generalized instrument resolution function

The instrumental resolution function defines the precision in reciprocal space with which $\mathbf{Q}$ is determined. Previous authors have developed expressions for the resolution function with various sources, monochromators and analyzers (Cooper & Nathans, 1967; Pynn, Fuji & Shirane, 1983; Cowley, 1987; Lucas, Gartstein & Cowley, 1989), but have always considered a spatially uniform incident beam. We relax this condition and treat a generalized resolution function, which depends on angular and spatial variables. We assume that the incident beam is imperfectly collimated and spatially nonuniform, but is monochromatic. This last approximation is not strictly correct, but we use it for simplicity and because we treat systems where the diffraction peak widths are broader than the resolution. We do not, therefore, expect this approximation to affect our results.

The details of our treatment are given in Appendix *B*, where we derive an expression for the generalized resolution function that combines both spatial and angular variables. Considerable simplification results when these variables can be decoupled and this results in the usual resolution function but a general form for the active sample area. This decoupling occurs when four conditions are met: (i) the sample surface is spatially homogenous; (ii) the probability of detecting a scattered X-ray involves little coupling between the position the X-ray scatters from and the direction it scatters into; (iii) the incident beam is sufficiently well collimated that its spatial profile does not change appreciably over the sample area; and (iv) the divergence of the incident beam is independent of position at the sample. Under these consitions, which are usually satisfied, the measured intensity is

$$I_m(\mathbf{Q}) = \mathscr{A}(\mathbf{Q}) \int d^3q\, \mathscr{R}(\mathbf{q})(d^2\sigma/d\Omega\, dA)(\mathbf{Q}+\mathbf{q}), \quad (2)$$

where $d^2\sigma/d\Omega\, dA$ is the differential scattering cross section per unit area on the surface and is an intrinsic function. The usual resolution function (*e.g.* for a spatially uniform incident beam) is

$$\mathscr{R}(\mathbf{q}) = (1/2k^3 \sin 2\theta) \int d\xi \mathscr{F}[\gamma_i(q_s, q_t), \beta_i(\xi, q_p)] \times \mathscr{D}[\gamma_f(q_s, q_t), \beta_f(\xi, q_p)], \quad (3)$$

where the symbols are defined in Table 1 and Appendix *B*. The active sample area $\mathscr{A}$ is the area illuminated by the incident beam and viewed by the detector and is defined in Appendix *B* [(72)]. We postpone discussion of this until § V.

In most experimental arrangements, the angular flux distribution and the detector probability are separable functions of γ and β: $\mathscr{F}(\gamma_i, \beta_i) = \mathscr{F}_\gamma(\gamma_i)\mathscr{F}_\beta(\beta_i)$ and $\mathscr{D}(\gamma_f, \beta_f) = \mathscr{D}_\gamma(\gamma_f)\mathscr{D}_\beta(\beta_f)$. In such cases, the resolution function is also separable, $\mathscr{R}(\mathbf{q}) = R_{st}(q_s, q_t)R_p(q_p)$, where

$$R_{st}(q_s, q_t) = (1/k^2 \sin 2\theta) \times \mathscr{F}_\gamma\{(1/2k)[(q_s/\cos\theta) - (q_t/\sin\theta)]\} \times \mathscr{D}_\gamma\{(1/2k)[(q_s/\cos\theta) + (q_t/\sin\theta)]\} \quad (4)$$

$$R_p(q_p) = (1/2k) \int d\xi \mathscr{F}_\beta\{(1/2)[\xi - (q_p/k)]\} \times \mathscr{D}_\beta\{(1/2)[\xi + (q_p/k)]\}.$$

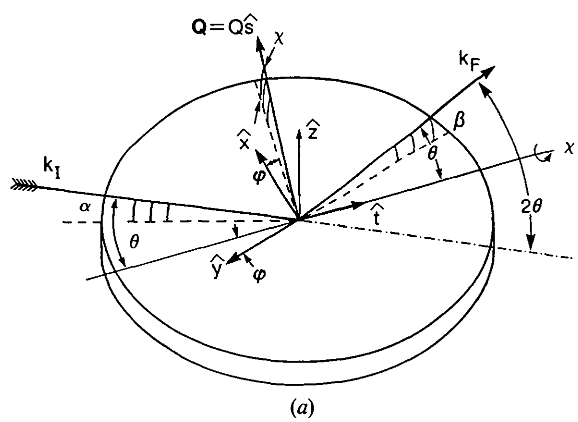

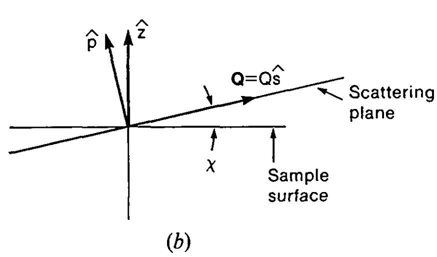

Fig. 1. (*a*) Illustration of surface X-ray scattering with the symmetric four-circle geometry. The incident X-ray wave vector is $\mathbf{k}_I$, the diffracted wave vector is $\mathbf{k}_F$ and the scattering vector is $\mathbf{Q}$. The scattering angle is 2θ, the sample angle is θ and the azimuthal or crystal rotation angle is φ (and is negative as drawn). The tilt along the plane bisecting the incoming and diffracted X-ray beams is the polar angle χ. The incidence and exit angles are α and β. The sample and scattering plane coordinate systems are described, respectively, by $\hat{\mathbf{x}}$, $\hat{\mathbf{y}}$ and $\hat{\mathbf{z}}$ (the sample normal), and by $\hat{\mathbf{s}}$, $\hat{\mathbf{t}}$ and $\hat{\mathbf{p}}$ ($\hat{\mathbf{p}}$ is not shown). (*b*) Geometry in the plane perpendicular to the sample surface and the scattering plane. Note that $\hat{\mathbf{t}}$ is perpendicular to the plane of the page.

C. Application to surface X-ray scattering

The resolution function can be represented by a resolution volume, which is the volume in reciprocal space enclosed by the 50% contour of the resolution function. We denote the full width at half-maximum (FWHM) of the resolution volume along its longest axis in the scattering plane by ΔQ_{st} and the FWHM perpendicular to the scattering plane as ΔQ_p. Typically, ΔQ_{st} is ~0.0005 Å^{-1} for high-resolution instruments and ~0.01 Å^{-1} for lower-resolution instruments. To increase count rates for surface scattering experiments, the angular acceptance of the detector perpendicular to the scattering plane is usually coarse,

Table 1. *List of symbols*

Symbol	Definition
a	Area of surface unit cell
$\mathcal{A}(\mathbf{Q})$	Active sample area, including X-ray absorption [(2) and (35)]
b	Width of squared Lorentzian function [Table 2]
$D_1\ (D_2)$	Spatial detector width perpendicular (parallel) to scattering plane [(38)]
$\mathcal{D}(\gamma_f, \beta_f)$	Angular dependent part of $\Delta(\gamma_f, \beta_f, \mathrm{r})$ [(68)]
$\mathcal{D}'(\mathbf{r})$	Function describing detector spatial acceptance and attenuation of scattered beam [(37)]
$E(Q_\parallel, Q_z)$	Integrated intensities in φ scans [(23) and (26)]
$E_{hk}(Q_z)$	$E(Q_\parallel, Q_z)$ evaluated at $Q_\parallel = G_{hk}$ [(28)]
$F(\mathbf{Q}, q_p)$	Intermediate function in evaluation of $I_m(\mathbf{Q})$ [(9) and (10)]
$F_{hk}(Q_z)$	Structure factor of hk surface rod [(20)]
$F_1\ (F_2)$	Rectangular incident-beam size perpendicular (parallel) to scattering plane [(39)]
$\mathcal{F}(\gamma_i, \beta_i)$	Angular dependent part of $\partial^2\Phi/\partial\gamma_i\partial\beta_i(\gamma_i, \beta_i, \mathbf{r})$ [(69)]
$\mathcal{F}'(\mathbf{r})$	Function describing spatial flux distribution of the incident beam, including attenuation [(36)]
$g(t)$	Indefinite integral of $G(t)$ [(19) and Table 2]
$G(Q_x - G_{hk})$	In-plane shape of $Q_\parallel$ scan at small Q_z [(12)]
$G_E(Q_\parallel - G_{hk})$	In-plane line shape of integrated intensities at small Q_z [(24)]
$\mathbf{G}_{hk}$	Surface reciprocal-lattice vector
G_G, G_L, G_{L2}	Constants in explicit expressions for $G(Q_x - G_{hk})$ [Table 2]
$H(\mathbf{Q}_\parallel, q_p, \chi)$	Intermediate function in evaluation of $F(\mathbf{Q}, q_p)$ [(10)]
$H_E(\mathbf{Q}_\parallel, q_p, \chi)$	Intermediate function in evaluation of $E(Q_\parallel - G_{hk})$ [(26)]
$I_m(\mathbf{Q})$	Experimentally measured diffraction intensity [(2)]
$I_0(\mathbf{Q})$	$r_0^2\mathcal{A}(\mathbf{Q})P/a$ [(9)]
$J(Q_x, \chi)$	Function describing broadening of $Q_\parallel$ scans with increasing Q_z [(18)]
$J_E(Q_z, \chi)$	Function describing broadening of $E(Q_\parallel, Q_z)$ with increasing Q_z [(27)]
$\mathbf{k}_I(\mathbf{k}_F)$	Average incident (diffracted) wave vector [(56) and Fig. 1]
$\mathbf{k}_i\ (\mathbf{k}_f)$	Incident (diffracted) wave vectors that deviate from $\mathbf{k}_I(\mathbf{k}_F)$ by γ_i and β_i (γ_f and β_f) [(59)]
L_s	Sample radius
$M(\mathbf{r})$	Sample shape function [(35) and (65)]
P	Polarization factor [(6)]
$\mathbf{Q}$	Scattering vector
$\mathbf{Q}_\parallel$	Component of $\mathbf{Q}$ parallel to surface
Q_x, Q_y, Q_z	Components of $\mathbf{Q}$ along $\hat{\mathbf{x}}, \hat{\mathbf{y}}$ and $\hat{\mathbf{z}}$
$\mathbf{q}$	Deviation of detected X-rays from $\mathbf{Q}$ [(60), (64) and (2)]
q_p, q_s, q_t	Component of $\mathbf{q}$ along $\hat{\mathbf{p}}, \hat{\mathbf{s}}$ and $\hat{\mathbf{t}}$ [(2) and (60)]
$\Delta Q_p\ (\Delta Q_{st})$	FWHM of resolution function along $\hat{\mathbf{p}}$ (longest axis in the scattering plane)
Q_e	Value of Q_z where S_z is evaluated [(17)]
r_0	Thompson radius
$\mathbf{r}$	Position on sample [(58), (63) and (35)]
$R(\mathbf{q})$	Generalized resolution function [(66)]
$R_{st}(q_s, q_t)$	Resolution function in the scattering plane [(4)]
$R_p(q_p)$	Resolution function perpendicular to the scattering plane [(4) and (5)]
$\mathcal{R}_{pk}$	Resolution correction for peak intensity measurements [(22)]
$\mathcal{R}_E\ (\mathcal{R}_\omega)$	Resolution correction for integrated intensities in φ scans (ω scans), [(28) and (33)]
$\mathcal{R}_G$	Resolution correction for integrated intensities in a Gaussian approximation for the resolution function [(34)]
$S_z(\mathbf{Q})$	Scattering function of diffraction rod perpendicular to surface [(6) and (7)]
$S_\parallel(\mathbf{Q}_\parallel)$	Scattering function of diffraction rod parallel to surface [(6) and (7)]
$t^+\ (t^-)$	Positive (negative) integration limit; $Q_x - G_{hk} \pm (\sin\chi\Delta Q_p/2)$ [(16)]
$\hat{\mathbf{p}}, \hat{\mathbf{s}}, \hat{\mathbf{t}}$	Unit vectors perpendicular to scattering plane, parallel to $\mathbf{Q}$ and perpendicular to $\mathbf{Q}$, but in scattering plane [(55) and Fig. 1]
$V(x)$	Function $= 1$ for $x < 1$, $= 0$ for $x > 1$
$W(x)$	Square-wave function $= 1$ for $\lvert x\rvert < 1/2$, $= \theta$ otherwise
w_0	In-plane FWHM of surface diffraction rod
$\hat{\mathbf{x}}, \hat{\mathbf{y}}(\hat{\mathbf{z}})$	Unit vectors parallel (perpendicular) to the sample surface [(55) and Fig. 1]
$\beta_i\ (\beta_f)$	Angular deviation of incident X-rays from $\mathbf{k}_I$ (detected X-rays from $\mathbf{k}_F$) out of the scattering plane [(59) and Fig. 1]
$\gamma_i\ (\gamma_f)$	Angular deviation of incident X-rays from $\mathbf{k}_I$ (detected X-rays from $\mathbf{k}_F$) in the scattering plane [(59) and Fig. 1]
$\Delta\beta_f\ (\Delta\gamma_f)$	Angular acceptance of detector out of (in) the scattering plane [(74) and (77)]
$\Delta(\gamma_f, \beta_f, \mathbf{r})$	Probability of detecting a scattered X-ray into the detector [(64)]
μ	Linear X-ray absorption coefficient
$\sigma_1\ (\sigma_2)$	Gaussian r.m.s. width of incident beam perpendicular (parallel) to scattering plane [(46)]
σ_G	r.m.s. width of Gaussian shaped $G(Q_x - G_{hk})$ [Table 2]
$\partial^2\sigma/\partial\Omega\partial A$	Differential X-ray scattering cross section per unit surface area [(2) and (6)]
$\Phi(\mathbf{r})$	Spatial flux density at sample [(63)]
Φ_0	Maximum spatial flux density at sample [(73)]
$\partial^2\Phi/\partial\gamma_i\partial\beta_i$	Angular distribution function of incident X-rays [(63)]
Ω	Angular velocity of a φ or ω scan [(23)]

$\Delta\beta_f \sim 10$–20 mrad. This is large compared to the incident beam's angular spread perpendicular to the scattering plane, $\Delta\beta_i \sim 2$–5 mrad and, therefore the detector acceptance determines the out-of-plane resolution ($\Delta Q_p \simeq k\Delta\beta_f \sim 0.1$ Å^{-1}). Thus, the resolution volume is much narrower in the scattering plane than perpendicular to it.

The anisotropic shape of the resolution function has important consequences in surface X-ray scattering. This is shown in Fig. 2, which illustrates the path of the resolution volume in a $Q_\parallel$ scan (constant Q_z) through a surface diffraction rod at G_{hk}. For small χ, the rod and the long part of the resolution volume are aligned and overlap for a small range in $Q_\parallel$; the resulting line shape is narrow. As χ increases, the rod and broad part of the resolution volume become misaligned, resulting in a broadening of the line shape and a concomitant reduction in the peak intensity (Robinson, 1988). If the rod intensity is approximately constant, the resulting line shape will be symmetric. If, however, there is significant variation in the intensity along the rod over $\Delta Q_z \sim \Delta Q_p \cos\chi$, then the line shape will be asymmetric. As illustrated in Figs. 2(a) and (b), this occurs because the resolution volume intersects the rod at smaller Q_z when $Q_\parallel < G_{hk}$ than when $Q_\parallel > G_{hk}$ and, as assumed above, the intensity variation with Q_z is significant.

To quantify this behavior, we must have more quantitative knowledge of the shape of the resolution function. In previous work, Robinson (1988) assumed the resolution function was a Gaussian function in the in-plane and out-of-plane directions. This is a good starting point, but it does not adequately describe the resolution function when wide slits are used to define the out-of-plane resolution, as is typical for surface scattering (Robinson, 1991). In this case, the resolution function has an out-of-plane shape that is approximately a square wave. For this reason, we approximate the out-of-plane resolution as

$$R_p(q_p) = (1/k)\,W(q_p/\Delta Q_p), \qquad (5)$$

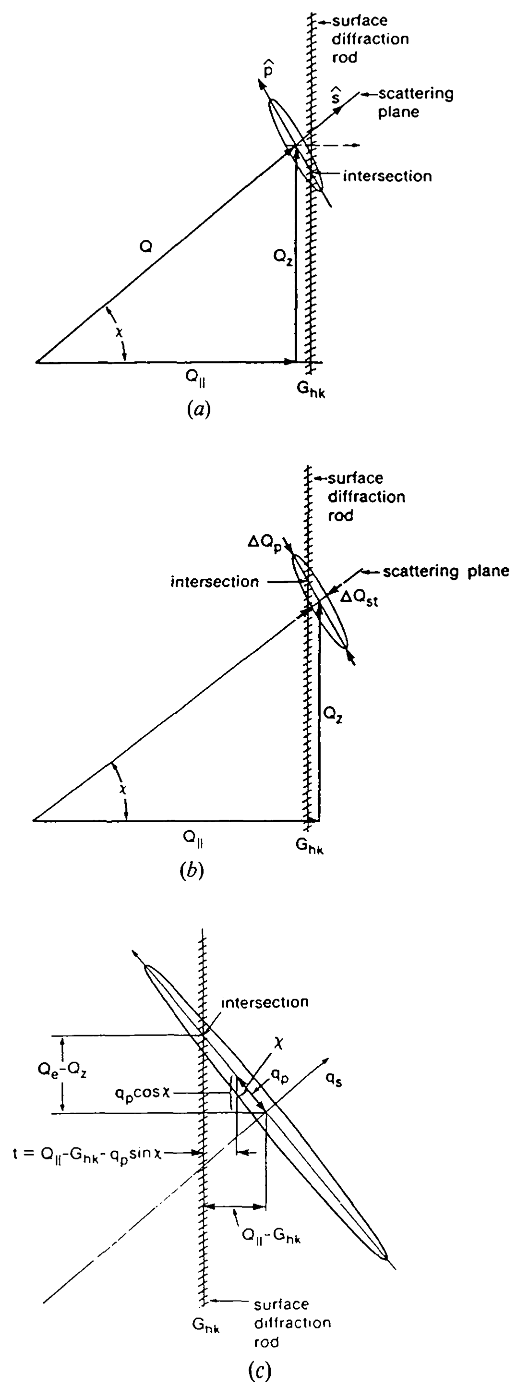

Fig. 2. The path of the resolution volume during a $Q_\parallel$ scan through a surface diffraction rod. The scattering plane is perpendicular to the page and intersects the page as shown by the line. The widths of the resolution volume along $\mathbf{Q}$ and perpendicular to the scattering plane are ΔQ_{st} and ΔQ_p and the resolution volume is shown by the ellipse. (*a*) Illustration of the overlap between the surface rod and the resolution volume for $Q_\parallel < G_{hk}$. The intersection occurs at a position along the rod that is smaller than Q_z. (*b*) The overlap for $Q_\parallel > G_{hk}$. The intersection occurs at a position larger than Q_z. (*c*) Expanded view of the region near the intersection of the rod and the resolution volume, which occurs at $Q_e = Q_z + (Q_\parallel - G_{hk})/\tan\chi$.

where $W(x)$ is a square wave function, $W(x) = 1$ for $-1/2 < x < 1/2$ and $W(x) = 0$ otherwise.

We assume that the scattering cross section can be separated into two parts:

$$d^2\sigma/d\Omega dA = (r_0^2 P/a) S_z(\mathbf{Q}) S_\parallel(\mathbf{Q}). \quad (6)$$

Here r_0 is the Thompson radius, a is the area of the surface unit cell, P is the polarization factor (Warren, 1969; Robinson, 1991; Feidenhans'l, 1989) and $S_z(\mathbf{Q})$ and $S_\parallel(\mathbf{Q}_\parallel)$ are the scattering functions of the rod perpendicular to and parallel to the surface, respectively:

$$S_z(\mathbf{Q}) = \left| \sum_{m=0}^{M} \sum_i f_{i,m}(Q) \exp(i\mathbf{Q}\cdot\mathbf{r}_{i,m}) \right|^2$$
$$S_\parallel(\mathbf{Q}_\parallel) = (1/N) \left| \sum_{n=1}^{N} \exp(i\mathbf{Q}_\parallel \cdot \mathbf{r}_n) \right|^2. \quad (7)$$

Here, $\mathbf{r}_n$ denotes the position of the nth surface unit cell; N is the number of surface unit cells; $f_{i,m}$ and $\mathbf{r}_{i,m}$ are the atomic form factor and the position of atoms i, m, respectively; and the sums on n, i and m are over the surface unit cells, the atoms in the surface unit cell and all the planes in the crystal (*e.g.* $M = 0$ for a monolayer and $M = \infty$ for a bulk crystal), respectively. For crystalline surfaces, $S_\parallel(\mathbf{Q})$ is sharply peaked at the surface reciprocal-lattice vectors $\mathbf{Q}_\parallel = \mathbf{G}_{hk}$. In contrast, $S_z(\mathbf{Q})$ does not have a strong variation with $\mathbf{Q}_\parallel$ and in the remainder of this section and in §§ III.*A* and *B* we drop the $\mathbf{Q}_\parallel$ dependence of S_z and write $S_z(Q_z)$ because here we consider $\mathbf{Q}_\parallel$ in a small range about $\mathbf{G}_{hk}$. Note that

$$\int dQ_x\, dQ_y S_\parallel(\mathbf{Q}) = 4\pi^2/a, \quad (8)$$

where the integration is over a range of about one Bragg rod. The assumption of separability made above [(6) and (7)] is for mathematical simplicity and will be approximately satisfied in many situations of interest. If this assumption is incorrect (*e.g.* vicinal surfaces), then the results of §§ III.*A*–*C* for peak intensity measurements are likely to be inaccurate. However, our results for integrated intensities in φ scans (§§ III.*D*–*F*) will still apply, provided the in-plane shape of $d^2\sigma/d\Omega\, dA$ does not change significantly for $0 \lesssim Q_z < 1$ Å^{-1}. Independent of this requirement, our results will apply for larger Q_z, because the broad direction of the resolution function effectively integrates (in-plane) over $d^2\sigma/d\Omega\, dA$ (see Appendix *E*.2).*

* Appendices *C*, *D*, *E* and *F* have been deposited with the British Library Document Supply Centre as Supplementary Publication No. SUP55868 (11 pp.). Copies may be obtained through The Technical Editor, International Union of Crystallography, 5 Abbey Square, Chester CH1 2HU, England.

Using the separability of $R(\mathbf{q})$ and $d^2\sigma/d\Omega dA$ [(4) and (7)], one obtains the measured intensity [(2)] as

$$\begin{aligned} I_m(\mathbf{Q}) &= I_0(\mathbf{Q}) \int dq_p\, R_p(q_p) F(\mathbf{Q}, q_p) \\ F(\mathbf{Q}, q_p) &= \int dq_s\, dq_t\, R_{st}(q_s, q_t) \\ &\quad \times S_z(Q_z + q_p \cos\chi + q_s \sin\chi) S_\parallel(Q'_x, Q'_y) \\ Q'_x &= Q_x + q_s \cos\varphi \cos\chi - q_t \sin\varphi \\ &\quad - q_p \cos\varphi \sin\chi \\ Q'_y &= Q_y + q_s \sin\varphi \cos\chi + q_t \cos\varphi \\ &\quad - q_p \sin\varphi \sin\chi, \end{aligned} \tag{9}$$

where $I_0(\mathbf{Q}) = r_0^2 \mathscr{A}(\mathbf{Q}) P/a$, φ is the crystal rotation angle and the transformation of $\mathbf{q}$ into sample coordinates is given in Appendix A. Because the width of $R_{st}(q_s, q_t)$ is small ($\Delta Q_{st} \sim 0.0005$–$0.01$ Å^{-1}) and $S_z(Q_z)$ varies slowly with Q_z, $F(\mathbf{Q}, q_p)$ can be accurately approximated by putting S_z before the integral and evaluating it at $q_s = 0$. This yields

$$\begin{aligned} F(\mathbf{Q}, q_p) &= S_z(Q_z + q_p \cos\chi) H(\mathbf{Q}_\parallel, q_p, \chi) \\ H(\mathbf{Q}_\parallel, q_p, \chi) &= \int dq_s\, dq_t\, R_{st}(q_s, q_t) S_\parallel(Q'_x, Q'_y). \end{aligned} \tag{10}$$

We use this approximation throughout the remainder of the paper.

III. Specific diffraction scans

We consider below three scans that are of particular utility in surface X-ray scattering. First, we discuss $Q_\parallel$ scans where φ and Q_z are held constant while $Q_\parallel$ is scanned through G_{hk}. Next, we consider rod scans, or scans of Q_z holding $\mathbf{Q}_\parallel$ constant. Last, we treat integrated intensities in φ scans (Q_z and $Q_\parallel$ constant). The goals of this section are to predict the Q_z dependence of the line shapes in $Q_\parallel$ scans and to obtain the ideal scattering function $S_z(Q_z)$ (the squared modulus of the structure factor) from the observed intensity. Details are presented in Appendices $C - F$.

A. $Q_\parallel$ scans at small Q_z

Without loss of generality, we consider the case where $\varphi = 0$ [*e.g.* $\mathbf{Q} = Q(\cos\chi\hat{\mathbf{x}} + \sin\chi\hat{\mathbf{z}})$]. From (9)–(11),

$$\begin{aligned} H(Q_x, q_p, \chi) &= \int dq_s\, dq_t\, R_{st}(q_s, q_t) \\ &\quad \times S_\parallel(Q_x + q_s \cos\chi - q_p \sin\chi; q_t). \end{aligned} \tag{11}$$

At small χ, we can neglect the slight χ dependence in this equation and $H(Q_x, q_p, \chi)$ will be independent of q_p. This is a good approximation when the error made by neglecting χ is small compared with the width of $H(Q_x, q_p, \chi)$: $\Delta Q_p \sin\chi \ll (w_0^2 + \Delta Q_{st}^2)^{1/2}$, where w_0 is the FWHM of $S_\parallel(Q_x, Q_y)$. With this approximation, the measured intensity [(9) and (10)] is

$$\begin{aligned} I_m(\mathbf{Q}) &= I_0(\mathbf{Q}) G(Q_x - G_{hk}) \\ &\quad \times \int dq_p\, R_p(q_p) S_z(Q_z + q_p) \\ G(Q_x - G_{hk}) &= \int dq_s\, dq_t\, R_{st}(q_s, q_t) S_\parallel(Q_x + q_s, q_t). \end{aligned} \tag{12}$$

All the Q_x dependence of $I_m(\mathbf{Q})$ is contained in $G(Q_x - G_{hk})$, which is sharply peaked at $Q_x = G_{hk}$ and has a FWHM of the order $(\Delta Q_{st}^2 + w_0^2)^{1/2}$ [because it is the convolution of $R_{st}(q_s, q_t)$ and $S_\parallel(Q_x, Q_y = 0)$]. Since $S_z(Q_z)$ is a slowly varying function, we approximate it as a constant within the integral in (12) and, using the square-wave expression for $R_p(q_p)$ [(5)], we obtain

$$I_m(\mathbf{Q}) = \left[\frac{I_0(\mathbf{Q}) \Delta Q_p}{k}\right] S_z(Q_z) G(Q_x - G_{hk}). \tag{13}$$

Thus, a $Q_\parallel$ scan at small Q_z has a peak intensity proportional to $S_z(Q_z)$ and directly measures the profile $G(Q_x - G_{hk})$.

B. $Q_\parallel$ scans at larger Q_z

We now consider larger χ, but still small enough that we can neglect the $\cos\chi$ dependence in the integral for $H(Q_x, q_p, \chi)$ [(11)]. This gives $H(Q_x, q_p, \chi) \simeq G(Q_x - q_p \sin\chi - G_{hk})$, with the result

$$F(\mathbf{Q}, q_p) = S_z(Q_z + q_p \cos\chi) G(Q_x - q_p \sin\chi - G_{hk}). \tag{14}$$

This is a major approximation of this subsection and we discuss its validity at the end of the subsection. Substituting the expression for $F(\mathbf{Q}, q_p)$ above and the square-wave form for $R_p(q_p)$ [(5)] into the expression for $I_m(\mathbf{Q})$ [(9)], we find

$$\begin{aligned} I_m(\mathbf{Q}) &= [I_0(\mathbf{Q})/k] \int_{-\Delta Q_p/2}^{\Delta Q_p/2} dq_p\, S_z(Q_z + q_p \cos\chi) \\ &\quad \times G(Q_x - q_p \sin\chi - G_{hk}). \end{aligned} \tag{15}$$

With reference to Fig. 2(c), this is the integral of the product of S_z and the low-Q_z line shape G along the line defining the center of the resolution volume. It is mathematically convenient to change variables to $t = Q_x - q_p \sin\chi - G_{hk}$, which gives

$$\begin{aligned} I_m(\mathbf{Q}) &= [I_0(\mathbf{Q})/k \sin\chi] \int_{t^-}^{t^+} dt\, G(t) \\ &\quad \times S_z\{Q_z + [(Q_x - G_{hk} - t)/\tan\chi]\}, \end{aligned} \tag{16}$$

where the integration limits are $t^\pm = Q_x - G_{hk} \pm (\sin\chi \Delta Q_p/2)$. Although it is straightforward to calculate this integral numerically if S_z is known, we can obtain insight into the peak shapes in $Q_\parallel$ scans by approximating S_z as constant over the integration range and evaluating it at the peak in $G(t)$. This is similar to the approximation used in calculating $F(\mathbf{Q}, q_p)$ in (10) and works because S_z does not vary appreciably over the integration range. When this range includes zero ($t^- < 0 < t^+$), the peak in $G(t)$ occurs at $t = 0$; otherwise, it occurs at t^+ (if $t^+ < 0$) or t^- (if $t^- > 0$). This is seen in Fig. 2(*c*) and we approximate this behavior with an error function and evaluate S_z at

$$Q_e = Q_z + (\Delta Q_p \cos\chi/2) \times \operatorname{erf}[\pi^{1/2}(Q_x - G_{hk})/\Delta Q_p \sin\chi]. \quad (17)$$

This form is computationally convenient and gives the correct limiting expressions when $Q_x - G_{hk} \to 0$ (*e.g.* $Q_e = Q_z + (Q_x - G_{hk})/\tan\chi$) and when $|Q_x - G_{hk}| \gg (\sin\chi \Delta Q_p/2)$ [*e.g.* $Q_e = Q_z \pm (\cos\chi \Delta Q_p/2)$]. With this approximation,

$$I_m(\mathbf{Q}) = I_0(\mathbf{Q}) S_z(Q_e) J(Q_x, \chi);$$
$$J(Q_x, \chi) = (1/k \sin\chi) \int_{t^-}^{t^+} G(t)\, \mathrm{d}t. \quad (18)$$

This expression for $I_m(\mathbf{Q})$ is an important result of this section. It shows how to account for changes in $Q_\parallel$ line shapes as Q_z increases with no *a priori* knowledge of the in-plane resolution function. One first uses $Q_\parallel$ scans at small Q_z to directly measure $G(t)$; this measured profile is then used to calculate $J(Q_x, \chi)$ and $I_m(\mathbf{Q})$, using (18). The function $J(Q_x, \chi)$ accounts for the broadening of peaks with increasing χ, whereas $S_z(Q_e)$ describes the asymmetry. For small χ, the integration range is small, $t^+ \simeq t^-$ and $J(Q_x, \chi) = (\Delta Q_p/k) G(Q_x - G_{hk})$; thus, $J(Q_x, \chi)$ and $I_m(\mathbf{Q})$ have the same sharply peaked line shape as G. As χ becomes larger, the integration range becomes larger and $J(Q_x, \chi)$ evolves into a broad relatively flat-topped function that is nonzero for $|Q_x - G_{hk}| \lesssim (\Delta Q_p \sin\chi)/2$. Thus, for large χ, $I_m(\mathbf{Q})$ is broad and if $S_z(Q_e)$ depends on Q_e over the range where $J(Q_x, \chi)$ is nonzero [$|Q_e - Q_z| < (\Delta Q_p/2)\cos\chi$], $I_m(\mathbf{Q})$ will be asymmetric.

It is useful to evaluate $I_m(\mathbf{Q})$ [(18)] for several specific $G(t)$, since this will illustrate some of the general features of the expression for $I_m(\mathbf{Q})$. Gaussian and Lorentzian shapes are chosen because they are analytically simple, while a Lorentzian squared is chosen because it fits our data for Ag(111). The results are summarized as

$$I_m(\mathbf{Q}) = [I_0(\mathbf{Q}) S_z(Q_e)/k \sin\chi][g(t^+) - g(t^-)], \quad (19)$$

where the functions $g(t)$ are the indefinite integrals of $G(t)$ and are given in Table 2. Here σ_G is the Gaussian root-mean-square (r.m.s.) width, b is the width of the Lorentzian (Lorentzian squared) and t^+ and t^- are given above. As shown in Appendix *D*.1, G_G, G_{L2} and G_L depend on w_0, 2θ, the sample mosaic, the acceptance of the detector and the spatial flux of the incident beam. If these do not vary appreciably over the rod measurement, we can approximate G_G, G_{L2} and G_L as constant. Appendix *D*.1 also shows that b and σ_G have a small dependence on χ that we do not consider.

To obtain $I_m(\mathbf{Q})$ [(18)], the major approximation of this section was the neglection of the $\cos\chi$ dependence in the expression for $H(Q_x, q_p, \chi)$ [(11)]. This is valid provided the error from this approximation is small compared with the width of G [*i.e.* $\Delta Q_{st}(1 - \cos\chi) \ll (w_0^2 + \Delta Q_{st}^2)^{1/2}$]. This will certainly be true when at least one of two conditions is met: (i) the in-plane resolution ΔQ_{st} is much smaller than the scattering-function width w_0; or (ii) $\cos\chi$ is not too different from 1. However, the expression for $I_m(\mathbf{Q})$ in (18) is valid under much more general conditions than this. As shown in Appendix *D*.1, (18) is an excellent approximation for essentially all χ. We expect the approximation to be less good (errors of ~15–20%) only for $\sin\chi \gtrsim (w_0^2 + \Delta Q_{st}^2)^{1/2}/2\Delta Q_{st}$ and then only in the small region

$$(\Delta Q_p \sin\chi)/2 - (w_0^2 + \Delta Q_{st}^2)^{1/2} \lesssim |Q_x - G_{hk}| \lesssim (\Delta Q_p \sin\chi)/2 + (w_0^2 + \Delta Q_{st}^2)^{1/2}.$$

C. Q_z scans

In the preceding subsections, we considered how the anisotropic shape of the resolution function causes a broadening of the line shape in $Q_\parallel$ scans. The concomitant reduction in the peak intensity must be accounted for when using measured intensities to calculate structure factors:

$$F_{hk}(Q_z) = \sum_{m=0}^{M} \sum_i f_{i,m}(Q) \exp(i\mathbf{G}_{hk} \cdot \mathbf{r}_{i,m}) \times \exp(iQ_z \hat{\mathbf{z}} \cdot \mathbf{r}_{i,m}). \quad (20)$$

The symbols are defined in § II.*C* and the structure factor is related to the scattering function by

$$S_z(\mathbf{G}_{hk}, Q_z) = |F_{hk}(Q_z)|^2. \quad (21)$$

In this and the following subsections, we discuss how to obtain the magnitude of the structure factor from measured intensities. We first consider Q_z scans, which measure the Q_z dependence of the peak intensity of the surface rod $I_{hk}(Q_z) \equiv I_m(\mathbf{G}_{hk}, Q_z)$. With reference to (18) and (21), we see that

$$I_{hk}(Q_z) = I_0(\mathbf{G}_{hk}, Q_z) J(G_{hk}, \chi) |F_{hk}(Q_z)|^2. \quad (22)$$

This states that a measurement along the surface rod yields an intensity that is just $|F_{hk}(Q_z)|^2$ scaled by a geometric factor $I_0(\mathbf{Q})$ and the function $J(G_{hk}, \chi)$. As with (18) for $I_m(\mathbf{Q})$, the expression above will be an excellent approximation for essentially all χ. Similar to Robinson (1988), we define the resolution correction $\mathcal{R}_{pk} = J(G_{hk}, \chi)$, which accounts for the

Table 2. *The indefinite integrals* $[g(t)]$ *and FWHM of the in-plane line shapes* $[G(t)]$ *that are Gaussian, Lorentzian and Lorentzian squared*

	Gaussian	Lorentzian	Lorentzian squared
$G(t)$	$(G_G/\sigma_G)\exp(-t^2/2\sigma_G^2)$	$G_L b/(b^2+t^2)$	$G_{L2}b^3/(b^2+t^2)^2$
$g(t)$	$[(2\pi)^{1/2}G_G/2]\,\mathrm{erf}\,(t/2^{1/2}\sigma_G)$	$G_L\tan^{-1}(t/b)$	$(G_{L2}/2)[tb/(t^2+b^2)+\tan^{-1}(t/b)]$
FWHM	$2^{3/2}(\ln 2)^{1/2}\sigma_G$	$2b$	$2(2^{1/2}-1)^{1/2}b$

intensity reduction caused by the anisotropic resolution function. The subscript pk indicates that this is for peak intensity measurements in Q_z scans. $\mathcal{R}_{pk}$ depends on the empirical function $G(Q_x-G_{hk})$ and so to calculate structure factors from Q_z scans one must first determine $G(Q_x-G_{hk})$ from $Q_\parallel$ scans at small Q_z.

D. φ scans at small Q_z

Peak intensity measurements of the surface rod are sensitive to possible changes in the mosaic structure of the rod at different Q_z. To minimize the impact of the mosaic structure, one measures the integrated intensities in ω or φ scans (Robinson, 1986, 1988; Feidenhans'l, 1989; Lucas *et al.*, 1988; Kashihara, Kimura & Harada, 1989; Sandy, Mochrie, Zehner, Huang & Gibbs, 1991; Ocko, Gibbs, Huang, Zehner & Mochrie, 1991), where the intensity is measured while either ω or φ is varied but Q_z and $Q_\parallel$ are constant. In this and the following subsection, we consider φ scans where in-plane detector resolution is not large ($\Delta Q_{st}\lesssim 0.05$ Å^{-1}) and not all the intensity along $Q_\parallel$ is collected. We postpone until § III.*F* treatment of the case where the in-plane detector resolution is sufficiently coarse for all the intensity along $Q_\parallel$ to be collected. Appendix *E* considers large Q_z where the broad direction of the resolution function effectively integrates $S_\parallel(\mathbf{Q}_\parallel)$ in $Q_\parallel$.

In this calculation, we use an approach similar to that of Warren (1969) [see also Robinson (1991) and Feidenhans'l (1989)] and denote the angular velocity of the φ scan as $\Omega=\mathrm{d}\varphi/\mathrm{d}t$. The intensity is integrated along $\mathbf{Q}_\parallel=Q_\parallel(\cos\varphi\hat{\mathbf{x}}+\sin\varphi\hat{\mathbf{y}})$ and for most samples the active area $\mathcal{A}(\mathbf{Q})$ is either independent of φ or varies so slowly that it can be approximated as constant. Making the same assumption that $\chi\simeq 0$ as in § III.*A* $[\Delta Q_p\sin\chi\ll(w_0^2+\Delta Q_{st}^2)^{1/2}]$ and using the expression for $I_m(\mathbf{Q})$ in (9) and (10), we obtain the integrated intensity

$$\begin{aligned}E(Q_\parallel,\ Q_z)&=(1/\Omega)\textstyle\int\mathrm{d}\varphi I_m(\mathbf{Q})\\&=[I_0(Q_\parallel,\ Q_z)/\Omega Q_\parallel]\textstyle\int\mathrm{d}q_p R_p(q_p)\\&\quad\times S_z(Q_z+q_p)G_E(Q_\parallel-G_{hk}),\end{aligned}\qquad(23)$$

where

$$\begin{aligned}G_E(Q_\parallel-G_{hk})&=\textstyle\int\mathrm{d}q_s\mathrm{d}q_t R_{st}(q_s,q_t)\int\mathrm{d}(Q_\parallel\varphi)\\&\quad\times S_\parallel\{[(Q_\parallel+q_s)\cos\varphi-q_t\sin\varphi];\\&\qquad[(Q_\parallel+q_s)\sin\varphi+q_t\cos\varphi]\}.\end{aligned}\qquad(24)$$

As in § III.*A*, we use the good approximation that $S_z(Q_z)$ is a slowly varying function to put this in front of the integral in (23). We also use the square-wave expression for $R_p(q_p)$ and obtain

$$\begin{aligned}E(Q_\parallel,Q_z)&=[I_0(Q_\parallel,Q_z)\Delta Q_p/k\Omega Q_\parallel]\\&\quad\times S_z(Q_z)G_E(Q_\parallel-G_{hk}).\end{aligned}\qquad(25)$$

The function $G_E(Q_\parallel-G_{hk})$ is analogous to $G(Q_x-G_{hk})$ and can be empirically obtained from the integrated intensities at small Q_z for different $Q_\parallel$ near G_{hk}.

E. φ scans at larger Q_z

For larger Q_z, we make the same approximations as in §§ III.*A* and *B*. Referring to the expression for $I_m(\mathbf{Q})$ in (9) and (10), we write

$$\begin{aligned}E(Q_\parallel,Q_z)&=[I_0(Q_\parallel,Q_z)/\Omega Q_\parallel]\textstyle\int\mathrm{d}q_p\,R_p(q_p)\\&\quad\times S_z(Q_z+q_p\cos\chi)H_E(Q_\parallel,\ Q_z,\ q_p)\\H_E(Q_\parallel,q_p,\chi)&=\textstyle\int\mathrm{d}q_s\,\mathrm{d}q_t\,R_{st}(q_s,q_t)\int\mathrm{d}(Q_\parallel\varphi)\\&\quad\times S_\parallel(Q'_x,Q'_y)\\Q'_x&=(Q_\parallel+q_s\cos\chi-q_p\sin\chi)\cos\varphi-q_t\sin\varphi\\Q'_y&=(Q_\parallel+q_s\cos\chi-q_p\sin\chi)\sin\varphi+q_t\cos\varphi.\end{aligned}\qquad(26)$$

Following § III.*B*, we assume that $\cos\chi$ can be approximated by 1 in the expressions above, with the result $H_E(Q_\parallel,q_p,\chi)\simeq G_E(Q_\parallel-q_p\sin\chi-G_{hk})$. Using this, the top equation above is analogous to (15) for $I_m(\mathbf{Q})$ and following arguments similar to those after (15), we have

$$\begin{aligned}E(Q_\parallel,Q_z)&=[I_0(Q_\parallel,Q_z)/2k\Omega\sin\theta\cos\chi]\\&\quad\times S_z(Q_e)J_E(Q_\parallel,\chi);\end{aligned}\qquad(27)$$

$$J_E(Q_\parallel,\chi)=(1/k\sin\chi)\int_{t^-}^{t^+}G_E(t)\,\mathrm{d}t,$$

where we have used $Q_\parallel=2k\sin\theta\cos\chi$. To obtain the structure factor, we consider $E(Q_\parallel,Q_z)$ at the peak of the surface rod ($Q_\parallel=G_{hk}$):

$$\begin{aligned}E_{hk}(Q_z)&=[I_0(\mathbf{G}_{hk},Q_z)/\Omega]|F_{hk}(Q_z)|^2\\&\quad\times[(1/2k^2\sin\alpha\cos\chi)\\&\quad\times\int_{-(\sin\chi\Delta Q_p)/2}^{(\sin\chi\Delta Q_p)/2}G_E(t)\,\mathrm{d}t].\end{aligned}\qquad(28)$$

As with the expressions for $I_m(\mathbf{Q})$ in § III.*B*, the two equations above are excellent approximations for essentially all χ (see also Appendix *D*.1). The term in brackets is $\mathcal{R}_E$, the resolution correction for integrated intensities in φ scans. For integrated intensities in ω scans, the $\cos\chi$ in this expression is absent and the resolution correction is $\mathcal{R}_\omega = \mathcal{R}_E \cos\chi$. The difference between $\mathcal{R}_\omega$ and $\mathcal{R}_E$ is due to the different scan trajectories in reciprocal space.

To calculate $|F_{hk}(Q_z)|$ using $\mathcal{R}_E$, it is necessary to determine $G_E(Q_\parallel - G_{hk})$ from measurements of the integrated intensities at low Q_z, as described above. This procedure is, unfortunately, tedious and time consuming. However, in some cases to be described below, $G_E(Q_\parallel - G_{hk})$ is approximately proportional to $G(Q_x - G_{hk})$ and this can be used instead to calculate $\mathcal{R}_E$ (to within a constant). Since $G(Q_x - G_{hk})$ is simply measured with a few $Q_\parallel$ scans at small Q_z, proportionality between $G_E(Q_\parallel - G_{hk})$ and $G(Q_x - G_{hk})$ results in a tremendous simplification.

One such condition where $G_E(Q_\parallel - G_{hk})$ is proportional to $G(Q_x - G_{hk})$ is if the in-plane scattering function separates into longitudinal and transverse components: $S_\parallel(Q_x, Q_y) \simeq S_x(Q_x)S_y(Q_y)$. When this is true,

$$\begin{aligned} G_E(Q_\parallel - G_{hk}) &= \int \mathrm{d}q_s\, \mathrm{d}q_t\, R_{st}(q_s, q_t) \\ &\quad \times S_x(Q_\parallel + q_s) \int \mathrm{d}(Q_\parallel\varphi) S_y(Q_\parallel\varphi + q_t) \\ &= c_1 \int \mathrm{d}q_s\, \mathrm{d}q_t\, R_{st}(q_s, q_t) S_x(Q_\parallel + q_s) \end{aligned} \tag{29}$$

and

$$G(Q_x - G_{hk}) = \int \mathrm{d}q_s\, \mathrm{d}q_t\, R_{st}(q_s, q_t) S_x(Q_x + q_s) S_y(q_t), \tag{30}$$

where we have neglected the curvature in the Ewald sphere ($\varphi \ll 1$) and second-order terms in the small quantities φ, q_p and q_s. That the second integral in the top equation of (29) is just a constant (c_1) follows from the definition of $S_\parallel(Q_x, Q_y)$ [(7)]. If $S_y(q_t)$ is approximately constant over the range in q_t where $R_{st}(q_s, q_t)$ is large (*e.g.* the transverse width of the surface diffraction is broader than the resolution), then these equations show that $G_E(Q_\parallel - G_{hk})$ is approximately proportional to $G(Q_x - G_{hk})$: $G_E(Q_\parallel - G_{hk}) \simeq [c_1/S_y(0)]G(Q_x - G_{hk})$. Alternatively, if R_{st} is separable, $R_{st}(q_s, q_t) \simeq R_s(q_s)R_t(q_t)$, we have

$$\begin{aligned} G_E(Q_\parallel - G_{hk}) &= c_1[\int \mathrm{d}q_t\, R_t(q_t)] \\ &\quad \times [\int \mathrm{d}q_s\, R_s(q_s) S_x(Q_\parallel + q_s)] \\ G(Q_x - G_{hk}) &= [\int \mathrm{d}q_t\, R_t(q_t) S_y(q_t)] \\ &\quad \times [\int \mathrm{d}q_s\, R_s(q_s) S_x(Q_\parallel + q_s)] \end{aligned} \tag{31}$$

and $G_E(Q_\parallel - G_{hk})$ is again approximately proportional to $G(Q_x - G_{hk})$. The separability of $R_{st}(q_s, q_t)$ will approximately be satisfied, as long as the in-plane angular spread of the incident X-rays is not grossly different from the in-plane angular acceptance of the detector. This is not too restrictive and thus, in many cases, $G_E(Q_\parallel - G_{hk})$ will be approximately proportional to $G(Q_x - G_{hk})$ and $G(Q_x - G_{hk})$ can be used to calculate $\mathcal{R}_E$.

F. φ scans with poor detector resolution

Last, we consider measurements of the integrated intensity in φ scans when the in-plane detector resolution is sufficiently coarse that all the intensity along $Q_\parallel$ is collected for all Q_z. Because the in-plane peak width becomes quite large as χ increases, this type of scan requires very coarse in-plane detector resolution, $\Delta Q_{st} \gtrsim \Delta Q_p \sin\chi_{\max}$, where $\chi_{\max}$ is the maximum value of χ in the measurement. Consequently, this type of scan is not often used. The calculation of the total integrated intensity is outlined in Appendix *F* and the result is

$$\begin{aligned} E_{hk}(Q_z) &= \{4\pi^2 r_0^2 P \mathcal{A}(\mathbf{Q})/a^2\Omega\} |F_{hk}(Q_z)|^2 \\ &\quad \times [\Delta Q_p / k^3 \sin 2\theta \cos^2\chi]. \end{aligned} \tag{32}$$

Here, the resolution correction (the term in square brackets) is the same as the usual Lorentz factor (Warren, 1969), except for the $\cos^2\chi$ term, which results from the trajectory of the φ scan and the fact that the surface diffraction is a rod, not a point. At small Q_z, $\cos\chi = 1$ and this agrees with expressions obtained previously for surface diffraction at small Q_z (Feidenhans'l, 1989; Robinson, 1991).

IV. Discussion of the resolution correction and comparison with previous calculations

At this point, it is instructive to evaluate the resolution correction for typical experimental arrangements and to compare it with previous calculations (Robinson, 1988; Ocko, Gibbs, Huang, Zehner & Mochrie, 1991; Sandy, Mochrie, Zehner, Huang & Gibbs, 1991). We assume a Gaussian function for $G_E(Q_x - G_{hk})$ and consider the resolution correction for integrated intensities $\mathcal{R}_E$; but note that $\mathcal{R}_{pk}$ will have approximately the same form as $\mathcal{R}_E$ whenever $G_E(Q_\parallel - G_{hk})$ is proportional to $G(Q_x - G_{hk})$.

As shown in Appendix *D*.2, the resolution correction for this situation is

$$\mathcal{R}_E(\chi) = (1/\sin\alpha\cos\chi)\,\mathrm{erf}\,(\Delta Q_p \sin\chi / 2^{3/2}\sigma_G), \tag{33}$$

where σ_G is the r.m.s. width of $G_E(t)$ and we have neglected unimportant constant factors. Although σ_G actually has a small dependence on χ, this can be neglected to a good approximation. The dot-dashed line in Fig. 3 shows $\mathcal{R}_E$ using values of σ_G and ΔQ_p comparable to those for our experiments on Ag(111)

(Toney *et al.*, 1990; Toney, Gordon *et al.*, 1992) (see caption for details). For large Q_z, $\mathcal{R}_E$ falls off as $1/\sin\alpha\cos\chi$ and is small because the overlap between the surface diffraction rod and the resolution volume is small (see Fig. 2). In contrast, $\mathcal{R}_E$ is large when Q_z is small and, in particular, $\mathcal{R}_E(Q_z \simeq 0)$ is of the order $\Delta Q_p/\sigma_G$. To compare our results with previous calculations, we must use the resolution correction for ω scans $\mathcal{R}_\omega = \mathcal{R}_E \cos\chi$, since these calculations were for ω scans. The solid line in Fig. 3 shows $\mathcal{R}_\omega$ [using (33)] for our treatment.

Robinson (1988) calculated the resolution correction assuming $R(\mathbf{q})$ is Gaussian in both the in-plane and out-of-plane directions and found

$$\begin{aligned}\mathcal{R}_G = \{[2(w_0^2+\Delta q_v^2)^{1/2}\cos\theta]/\Delta q_r\Delta q_v\}\\ \times\{[(\Delta q_v\Delta q_r)/\sin 2\theta]/[w_0^2+(\Delta q_r\cos\chi)^2\\ +(\Delta q_v\sin\chi)^2]^{1/2}\},\end{aligned} \tag{34}$$

where the subscript G denotes the Gaussian approximation; Δq_v and Δq_r are the out-of-plane FWHM and in-plane FWHM of the resolution function, respectively; and the term $[2(w_0^2+\Delta q_v^2)^{1/2}\times\cos\theta]/\Delta q_r\Delta q_v$ normalizes $\mathcal{R}_G$ in the same manner as $\mathcal{R}_\omega(\mathcal{R}_G\sin\alpha = 1$ for large $Q_z)$. To be consistent with our definitions, the expression for $\mathcal{R}_G$ includes a Lorentz factor $(1/\sin 2\theta)$ as used by Robinson (1988). The dashed line in Fig. 3 shows $\mathcal{R}_G$ using the same FWHMs as in the calculation of $\mathcal{R}_\omega$ (see caption). The two forms for the resolution correction are similar for large Q_z, but differ for $Q_z \lesssim 1$ Å^{-1}.

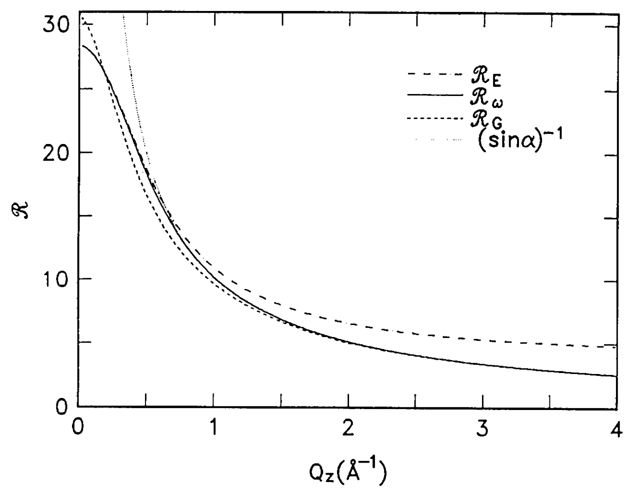

Fig. 3. Different calculations of the resolution correction $\mathcal{R}$ for a $(10Q_z)$ CTR from Ag(111). The dot–dashed line shows $\mathcal{R}_E$ for integrated intensities in φ scans when the resolution function out of the scattering plane has a square-wave shape and the in-plane line shape is a Gaussian function [(33)]. The widths of the resolution function and the surface diffraction peak are $\Delta Q_p = 0.048$ and $\sigma_G = 0.0027$ r.l.u. (reciprocal-lattice units). These are comparable to the widths we have found for Ag(111) (see § VI and Fig. 6). The solid line shows $\mathcal{R}_\omega = \mathcal{R}_E\cos\chi$, the resolution correction for ω scans. The dashed line shows $\mathcal{R}_G$ calculated with the assumption of a Gaussian-shaped resolution function both parallel and perpendicular to the scattering plane [(34)]. To compare this with $\mathcal{R}_\omega$, we have set the out-of-plane FWHM as $\Delta q_v = \Delta Q_p = 0.048$ r.l.u., the in-plane FWHM as $\Delta q_r = \Delta Q_{st} = 0.0021$ r.l.u. and the FWHM of the surface diffraction peak as $w_0 = 0.0061$ r.l.u. The dotted line shows the large-χ limit of $\mathcal{R}(=1/\sin\alpha)$, as calculated by Sandy, Mochrie, Zehner, Huang & Gibbs (1991) and Ocko, Gibbs, Huang, Zehner & Mochrie (1991) and in Appendix E.

In Sandy, Mochrie, Zehner, Huang & Gibbs (1991) and Ocko, Gibbs, Huang, Zehner & Mochrie (1991), the resolution correction for Q_z scans has been calculated when χ is large [*i.e.* $\Delta Q_p\sin\chi \gg (w_0^2+\Delta Q_{st}^2)^{1/2}$] and when the in-plane resolution is coarse compared to the width of the scattering function. For this case, the functional form for the resolution correction is simply $1/\sin\alpha$ and is shown by the dotted line in Fig. 3. This agrees with $\mathcal{R}_\omega$ for most χ, but differs for $Q_z \lesssim 0.5$ Å^{-1}. One can use (33) to estimate the value of χ where the $1/\sin\alpha$ form is no longer valid and if we permit a 10% error, this is $\chi = \sin^{-1}(3.31\sigma_G/\Delta Q_p)$. In Appendix E.1, we reproduce the results of Sandy, Mochrie, Zehner, Huang & Gibbs (1991) and Ocko, Gibbs, Huang, Zehner & Mochrie (1991) and also show that $\mathcal{R}_\omega$ has the same $1/\sin\alpha$ functional form for large χ.

V. Active sample area

We now turn our attention to the evaluation of the active sample area, defined in Appendix B [(72)] as

$$\mathcal{A}(\mathbf{Q}) = \int \mathrm{d}^2 r\, \mathcal{F}'(\mathbf{r}) M(\mathbf{r}) \mathcal{D}'(\mathbf{r}). \tag{35}$$

The factors inside the integral represent the probability of having an X-ray scattered at the sample position $\mathbf{r}$ and registered in the detector. This is governed by three effects: (1) the flux at $\mathbf{r}$, which depends on the spatial flux distribution of the incident beam and the attenuation of the incident beam in reaching $\mathbf{r}$, given by $\mathcal{F}'(\mathbf{r})$; (2) the probability of there being sample at $\mathbf{r}$, given by $M(\mathbf{r})$; and (3) the chance of detection, which depends on the detector spatial acceptance and the attenuation of the scattered beam, given by $\mathcal{D}'(\mathbf{r})$.

Because the incident spatial flux distribution is typically a separable function in the two directions perpendicular to the beam direction $\mathbf{k}_I$, we have

$$\mathcal{F}'(\mathbf{r}) = \mathcal{F}_1'(\mathbf{r}\cdot\hat{\mathbf{p}})\mathcal{F}_2'[\mathbf{r}\cdot(\mathbf{k}_I\times\hat{\mathbf{p}}/k)] \times \exp\Big[-\int_{\text{source}}^{\mathbf{r}} \mu(\mathbf{r}')\,\mathrm{d}r'\Big], \tag{36}$$

where the integral is evaluated along the path from the source to $\mathbf{r}$ and $\mu(\mathbf{r}')$ is the linear absorption coefficient. In this expression and those that follow, we use the convention that the subscripts 1 and 2 refer to directions perpendicular to and in the scattering plane, respectively. An analogous expression holds for the detector:

$$\mathscr{D}'(\mathbf{r}) = \mathscr{D}'_1(\mathbf{r}\cdot\hat{\mathbf{p}})\mathscr{D}'_2[\mathbf{r}\cdot(\mathbf{k}_F\times\hat{\mathbf{p}}/k)] \times \exp\left[-\int_{\mathbf{r}}^{\text{detector}} \mu(\mathbf{r}')\,\mathrm{d}r'\right], \quad (37)$$

where the integral is evaluated along the path from $\mathbf{r}$ to the detector. Appendix A gives the dot products in (36) and (37).

Although arbitrary sample shape functions $M(\mathbf{r})$ may be treated, we limit ourselves to the analytically simple case of a two-dimensional circular sample with radius L_s. With this geometry, $M(\mathbf{r}) = V(r/L_s)$, where $r=(x^2+y^2)^{1/2}$ is the sample radius and $V(x)=1$ for $x<1$, $V(x)=0$ otherwise. We also only consider the case of a uniformly absorbing material of linear absorption coefficient μ covering the sample to a thickness T. This is particularly relevant to our electrochemical experiments described in § VI. Other geometries, though, are easily treated. Given the assumptions above and taking $\varphi=0$ (which is done without loss of generality, because the sample is circular), the active area is

$$\begin{aligned}\mathscr{A}(\mathbf{Q}) = (\exp -2\mu T/\sin\alpha)\textstyle\int \mathrm{d}x\,\mathrm{d}y\, &\mathscr{F}'_1(-x\sin\chi) \\ &\times \mathscr{F}'_2(x\cos\theta\cos\chi - y\sin\theta) \\ &\times V[(x^2+y^2)^{1/2}/L_s]\,W(-x\sin\chi/D_1) \\ &\times W[(x\cos\theta\cos\chi + y\sin\theta)/D_2]. \quad (38)\end{aligned}$$

Here we have replaced the detector spatial acceptance with square-wave functions limiting the area viewed by the detector to D_1 and D_2 perpendicular and parallel to the scattering plane, respectively. It is usual to set D_1 larger than the beam size perpendicular to the scattering plane. This ensures that all the scattered X-rays are detected. Thus, the square-wave function involving D_1 is unity over the (x, y) of interest and can be dropped.

One can explicitly measure the spatial flux distribution of the incident beam by scanning a pin-hole across the beam at the sample position. This empirical function can then be introduced into (38) to determine $\mathscr{A}(\mathbf{Q})$. In what follows, however, we shall evaluate the expression above for two simple cases of practical interest. We first assume a uniform rectangular profile for the incident flux and calculate the active area for several limiting cases of incident-beam size, detector spatial acceptance and sample size. In the second example, we assume a Gaussian profile for the incident-flux distribution.

A. *Uniform rectangular flux distribution*

When the spatial flux density at the sample is a uniform rectangular beam of dimensions F_1 and F_2 perpendicular and parallel to the scattering plane, we have

$$\begin{aligned}\mathscr{A}(\mathbf{Q}) = [\exp(-2\mu T/\sin\alpha)]\textstyle\int \mathrm{d}x\,\mathrm{d}y\, &W(-x\sin\chi/F_1) \\ &\times W[(x\cos\theta\cos\chi - y\sin\theta)/F_2] \\ &\times V[(x^2+y^2)^{1/2}/L_s] \\ &\times W[(x\cos\theta\cos\chi + y\sin\theta)/D_2]. \quad (39)\end{aligned}$$

The integral in this equation represents the intersection of three areas, as illustrated schematically in Fig. 4. These areas are (1) the incident spatial flux, given by the first two square-wave (or W) functions; (2) the sample size, given by the V function; and (3) the detector acceptance area, defined by the final W function. The integral can be evaluated for an arbitrary situation, but we consider cases where the incident-beam size defines the active sample area along the direction perpendicular to the beam. This requires that the projected incident-beam size in this direction is smaller than both the sample extent and the detector spatial acceptance projected onto the sample surface: $F_2\cos\alpha/\cos\chi \ll 2L_s$ and $D_2\cos\alpha/\cos\chi$. This is usually the case in surface X-ray scattering (as long as χ is not near 90°). Below, we treat three cases where along the incident beam $\mathscr{A}$ is determined by (1) the incident-beam size, (2) the detector spatial acceptance or (3) the sample size.

(1) *Limiting incident-beam size.* The projected length of the incident beam onto the sample is smaller than both the sample extent and the projection of the detector spatial acceptance onto the sample. This requires

$$F_1(\cos^2\theta\cos^2\chi + \sin^2\theta)^{1/2}/\sin\alpha \lesssim 2L_s$$

and

$$F_1/\sin\alpha \lesssim b_2/\cos\chi\sin 2\theta, \quad (40)$$

which can be the case if χ and 2θ are not too small. The active area is the area of the incident flux parallelogram (see Fig. 4a) and

$$\begin{aligned}\mathscr{A}(\mathbf{Q}) &= [\exp(-2\mu T/\sin\alpha)]\textstyle\int \mathrm{d}x\,\mathrm{d}y\, W(-x\sin\chi/F_1) \\ &\quad\times W[(x\cos\theta\cos\chi - y\sin\theta)/F_2] \\ &= (F_1F_2/\sin\alpha)[\exp(-2\mu T/\sin\alpha)]. \quad (41)\end{aligned}$$

(2) *Limiting incident-beam size and detector spatial acceptance.* In this common experimental configuration, the spatial acceptance of the detector defines the active area along the length of the incident beam. This situation is shown in Fig. 4(b) and requires that the projected detector spatial acceptance is smaller than both the projected incident-beam length and the sample extent:

$$D_2(\cos^2\theta\cos^2\chi + \sin^2\theta)^{1/2}/\cos\chi\sin 2\theta \lesssim 2L_s$$

and

$$D_2/\cos\chi\sin 2\theta \lesssim F_1/\sin\alpha. \quad (42)$$

This can be the case for small χ but not too small 2θ and

$$\mathscr{A}(\mathbf{Q}) = [\exp(-2\mu T/\sin\alpha)] \int dx\, dy \times W[(x\cos\theta\cos\chi - y\sin\theta)/F_2] \times W[(x\cos\theta\cos\chi + y\sin\theta)/D_2] = (F_2 D_2/\sin 2\theta\cos\chi)[\exp(-2\mu T/\sin\alpha)]. \tag{43}$$

(3) *Limiting incident-beam size and sample size.* Here, the sample size limits the active area along the length of the incident beam. Thus, the sample extent is smaller than both the projected detector spatial acceptance and the projected incident-beam length:

$$2L_s \lesssim F_1(\cos^2\theta\cos^2\chi + \sin^2\theta)^{1/2}/\sin\alpha$$

and

$$2L_s \lesssim D_2(\cos^2\theta\cos^2\chi + \sin^2\theta)^{1/2}/\cos\chi\sin 2\theta, \tag{44}$$

which applies for small χ but not too large 2θ. This configuration is shown in Fig. 4(c) and

$$\mathscr{A}(\mathbf{Q}) = [\exp(-2\mu T/\sin\alpha)] \int dx\, dy \times V[(x^2+y^2)^{1/2}/L_s] \times W[(x\cos\theta\cos\chi - y\sin\theta)/F_2] = 2L_s F_2/(\cos^2\theta\cos^2\chi + \sin^2\theta)^{1/2} \times [\exp(-2\mu T/\sin\alpha)]. \tag{45}$$

B. Gaussian flux distribution

We now consider the case where the incident spatial flux distribution has a smoothly varying shape rather than the sharp form assumed above. This is appropriate for focusing optics when tightly set slits are not used to define the beam size. We further assume that the spatial flux distribution is a Gaussian function, since this is appropriate to our measurements. The

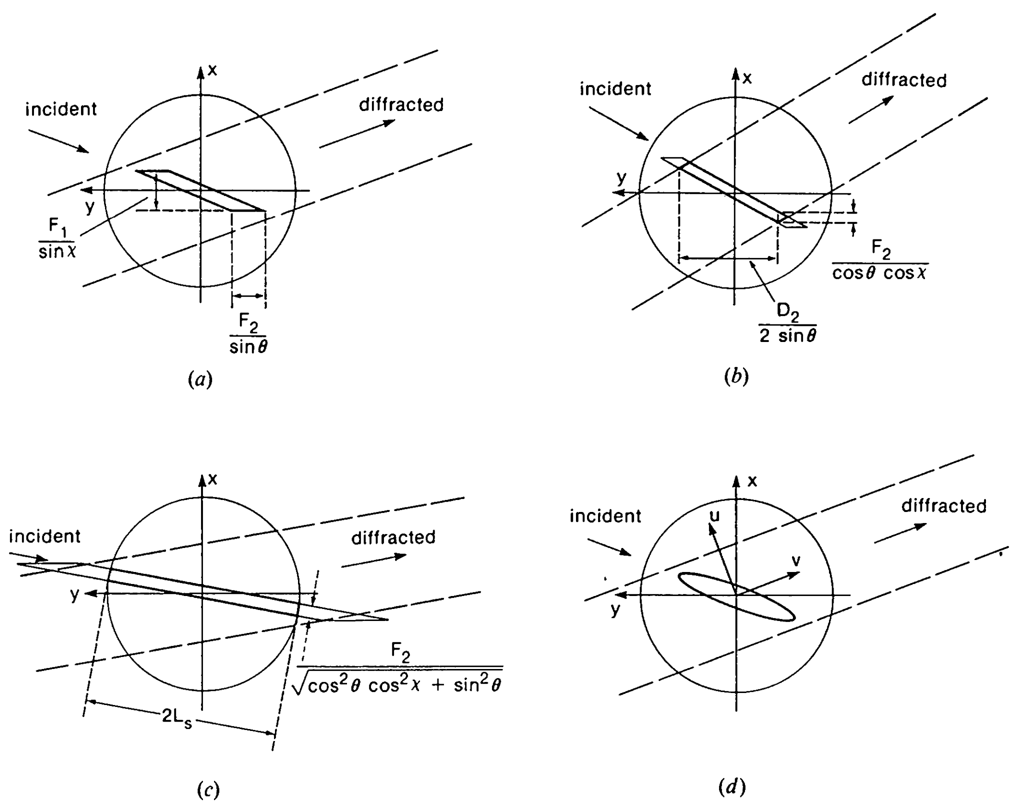

Fig. 4. Illustration of the active sample area $\mathscr{A}$, the area of the sample that is illuminated by the incident beam and viewed by the detector. The case of a rectangular incident beam is is shown in (a), (b) and (c), while (d) corresponds to a Gaussian incident beam. The circular sample has a radius L_s and the area enclosed by the long-dashed lines is that viewed by the detector. In (a), (b) and (c), the parallelogram is the area illuminated by the incident beam and the region enclosed by the bold lines is the active area. (a) Limiting incident-beam size (case 1). The active area is the product of the base and height of the incident-beam parallelogram: $(F_2/\sin\theta)\times(F_1/\sin\chi)$. ($b$) Limiting incident-beam size and detector spatial acceptance (case 2). The active area is the product of the base and height of the incident-beam parallelogram as cut off by the detector: $[F_2/\cos\theta\cos\chi]\times(D_2/2\sin\theta)$. ($c$) Limiting incident-beam size and sample size (case 3). The active area is the product of the base and height of the incident-beam parallelogram as cut off by the sample: $[F_2/(\cos^2\theta\cos^2\chi+\sin^2\theta)^{1/2}]\times 2L_s$. ($d$) Gaussian incident beam. The ellipse represents a contour of constant spatial flux density.

generalization to other functional forms is straightforward.

With these assumptions, the incident spatial flux distribution is

$$\begin{aligned}\mathscr{F}'(\mathbf{r}) &= \exp[-(\mathbf{r}\cdot\hat{\mathbf{p}})^2/2\sigma_1^2]\\ &\quad\times\exp\{-[\mathbf{r}\cdot(\mathbf{k}_I\times\hat{\mathbf{p}}/k)]^2/2\sigma_2^2\}\\ &\quad\times[\exp(-\mu T/\sin\alpha)]. \qquad (46)\end{aligned}$$

where σ_1 and σ_2 are the r.m.s. widths of the incident beam perpendicular and parallel to the scattering plane. The physical situation that results from this spatial flux distribution is similar to that for the rectangular beam. However, the bold lines in Fig. 4 are no longer sharp boundaries, but represent the width of a smooth distribution. We evaluate $\mathscr{A}$ for the case where the projected detector size is smaller than the sample length [(42), see Fig. 4*d*] and later give results for the opposite situation. From (38) and (46), we have

$$\begin{aligned}\mathscr{A}(\mathbf{Q}) &= \int dx\, dy \exp[-(x\sin\chi)^2/2\sigma_1^2]\\ &\quad\times\exp[-(x\cos\theta\cos\chi - y\sin\theta)^2/2\sigma_1^2]\\ &\quad\times W[(x\cos\theta\cos\chi + y\sin\theta)/D_2], \qquad (47)\end{aligned}$$

where we have dropped the absorption factor for brevity but will include it at the end of the calculation. To evaluate this integral, we change variables to

$$\begin{aligned}u &= (x\cos\theta\cos\chi + y\sin\theta)/(\cos^2\theta\cos^2\chi + \sin^2\theta)^{1/2}\\ v &= (x\sin\theta - y\cos\theta\cos\chi)/(\cos^2\theta\cos^2\chi + \sin^2\theta)^{1/2}, \qquad (48)\end{aligned}$$

with the result

$$\begin{aligned}\mathscr{A}(\mathbf{Q}) &= \int du\, W[u(\cos^2\theta\cos^2\chi + \sin^2\theta)^{1/2}/D_2]\\ &\quad\times\int dv \exp(-\{[x(u,v)\sin\chi]^2/2\sigma_1^2\}\\ &\quad-\{[x(u,v)\cos\theta\cos\chi\\ &\quad- y(u,v)\sin\theta]^2/2\sigma_1^2\}), \qquad (49)\end{aligned}$$

where $x(u, v)$ and $y(u, v)$ are the inverse of the transformations given in (48). The integration range for u is determined by the W function and is $\pm D_2' = \pm D_2/2(\cos^2\theta\cos^2\chi + \sin^2\theta)^{1/2}$. The integration range over v can be taken as infinite because v is orthogonal to u and $\mathbf{k}_F$ (see Fig. 4*d*) and since we have assumed that the sample is much larger than the incident-beam size ($L_s \gg \sigma_1, \sigma_2$). Thus,

$$\begin{aligned}\mathscr{A}(\mathbf{Q}) &= \int\limits_{-D_2'}^{D_2'} du \int\limits_{-\infty}^{\infty} dv \exp\left(-\left\{\frac{[x(u,v)\sin\chi]^2}{2\sigma_1^2}\right\}\right.\\ &\quad\left.-\left\{\frac{[x(u,v)\cos\theta\cos\chi - y(u,v)\sin\theta]^2}{2\sigma_1^2}\right\}\right)\\ &= (2\pi\sigma_1\sigma_2/\sin\alpha)[\exp(-2\mu T/\sin\alpha)]\\ &\quad\times\operatorname{erf}\{(D_2\sin\alpha/2^{3/2}\sigma_1\cos\chi\sin 2\theta)\\ &\quad\times[1 + (\sigma_2^2\tan^2\chi/4\sigma_1^2\cos^2\theta)]^{-1/2}\}, \qquad (50)\end{aligned}$$

where we have included the absorption factor in the last line and have skipped the algebraically tedious details.

Equation (50) leads to identical results as the uniform rectangular distribution in two limiting cases. First, when the projected beam size is much smaller than the projection of the detector spatial acceptance [*i.e.* $\sigma_1/(\sin\alpha) \ll D_2/(\cos\chi\sin 2\theta)$], the argument of the error function is large and $\mathscr{A} = (2\pi\sigma_1\sigma_2/\sin\alpha)\exp(-2\mu T/\sin\alpha)$. If we identify the beam widths as $F_i = (2\pi)^{1/2}\sigma_i$ (with $i = 1, 2$), this is precisely the expression given in (41) for a rectangular beam under the same limiting conditions. Second, when the opposite situation holds [*i.e.* $\sigma_1/(\sin\alpha) \gg D_2/(\cos\chi\sin 2\theta)$], the argument of the error function is small and

$$\mathscr{A} = [(2\pi)^{1/2}\sigma_2 D_2/(\cos\chi\sin 2\theta)]\exp(-2\mu T/\sin\alpha),$$

which is the same as for a rectangular beam under the same conditions [(43)].

In this subsection, we have assumed that the sample length is larger than the projected length viewed by the detector. If the opposite is true, then to evaluate $\mathscr{A}$ we follow the procedure given above except that W is replaced by V in (49). As a consequence, one of the variables we change to is along the projection of $\mathbf{k}_I$ onto the sample surface. The integration over this variable is from $-L_s$ to $+L_s$, while the integration over the orthogonal variable runs from $-\infty$ to $+\infty$. The result is that $D_2/(\cos\chi\sin 2\theta)$ should be replaced by $L_s/[(\sin^2\theta + \cos^2\chi\cos^2\theta)^{1/2}]$ in (50).

VI. Application to Ag(111)

We now apply the results of the previous sections to data we have obtained on Ag(111) electrode surfaces. These data consist of $Q_\parallel$ and Q_z scans and were taken from Ag(111) substrates that were either 'bare' or covered with an incommensurate monolayer of thallium (Toney *et al.*, 1990; Toney, Gordon *et al.*, 1992).

A. Experimental aspects and crystal truncation rod scattering

The data were collected at the National Synchrotron Light Source (NSLS) on beam line X20*A*. An incident X-ray energy of 9997 eV ($\lambda = 1.240$ Å) was selected using an Si(111) double monochromator. Approximately 4 mrad of X-radiation were collected from a bending magnet and focused onto the sample. By scanning a pinhole across the incident beam, we measured the spatial flux distribution of the incident beam at the sample and found that this could be approximated by a Gaussian function with r.m.s. widths $\sigma_2 = 0.33$ and $\sigma_1 = 0.73$ mm (vertical and horizontal, respectively). The diffracted beam was analyzed with 1 mrad Soller slits ($\Delta Q_{st} \simeq 0.005$ Å^{-1}) and the acceptance of the diffracted beam out of the scattering plane was defined by wide slits to be $\simeq 24$ mrad. The sample was aligned using bulk reflections and data were obtained in the symmetric four-circle mode (Busing & Levy, 1967). The Ag(111) substrates were epitaxially grown thin films of silver vapor deposited onto freshly cleaved mica (Samant, Toney, Borges, Blum & Melroy, 1988*a*, *b*). They had a diameter of $2L_s = 21$ mm and showed both *ABC* and *CBA* stacking (Toney *et al.*, 1990). During the measurements, the substrates were covered with a thin ($\lesssim 30\,\mu$m) layer of electrolyte. For the data presented below, the reciprocal lattice is indexed relative to the pseudohexagonal cell with $a^* = 2.511$ and $c^* = 0.8878$ Å^{-1}. Other experimental details can be found in Toney, Gordon *et al.* (1992).

In the *Introduction*, we discussed diffraction from a 2D crystal and surfaces of 3D crystals. Recall that for crystal truncation rods (CTRs) the structure factor varies significantly with Q_z and the variations contain information about the surface morphology. For a crystal surface that has atomic-scale roughness (*e.g.* steps), Robinson (1986) introduced a convenient real-space model to describe the CTR structure factor. This model allows partially filled substrate layers with a fractional occupancy β per layer ($0 < \beta < 1$) and with it the CTR structure factor for the (111) surface of a f.c.c. crystal is

$$\begin{aligned} S_z(Q_z) &= |F_{hk}(Q_z)|^2 \\ &= [(1-\beta)^2/(1+\beta^2 - 2\beta\cos S)] \\ &\quad \times |f_s(Q)/(1-\exp iS)|^2, \end{aligned} \tag{51}$$

where $S = (2\pi/3)(h-k) + CQ_z$, C is the spacing between (111) planes and $f_s(Q)$ is the atomic form factor of the substrate atoms. Since this model adequately describes our data for Ag(111) (Toney *et al.*, 1990), we use it hereafter.

B. Resolution-function effects in $Q_\parallel$ scans

Fig. 5 shows $Q_\parallel$ scans of a silver CTR at several Q_z, when no thallium is adsorbed on the silver surface. There are Bragg peaks at both $Q_z = 1$ and $Q_z = 2$ reciprocal-lattice units (r.l.u.) because the thin-film substrates have both *ABC* and *CBA* stacking [*i.e.* the data contain contributions from the ($10Q_z$) and ($01Q_z$) CTRs (Toney *et al.*, 1990)]. As Fig. 5 shows, at small Q_z the line shape is narrow, but at larger Q_z it broadens and becomes dramatically asymmetric. This behavior was qualitatively explained in § III.*B*. To calculate quantitatively the $Q_\parallel$ line shapes in Fig. 5, we use (16) from § III.*B*, where, for our data, $G(Q_x - G_{hk})$ is a squared Lorentzian. Dropping constant factors, we have

$$\begin{aligned} I_m(\mathbf{Q}) = (\mathscr{A}/\sin\chi) \int_{t^-}^{t^+} \mathrm{d}t\, [1/(b^2+t^2)^2] \\ \times S_z\{Q_z + [(Q_x - G_{hk} - t)/\tan\chi]\}, \end{aligned} \tag{52}$$

where $t^{\pm} = Q_x - G_{hk} \pm (\sin\chi\Delta Q_p/2)$ and S_z is given in (51). This expression can be simplified and the integral eliminated if we approximate S_z as constant, as was done to obtain (18); here, however, we evaluate the integral numerically, since this is slightly more accurate.

The solid lines in Fig. 5 show least-squares fits to the $Q_\parallel$ line shapes using the expression above. The roughness factor β (0.08), the X-ray absorption due to the material covering the silver electrode μT (0.031) and the CBA stacking fraction (0.38) were taken from fits to the CTR intensity described in Toney *et al.* (1990). For each diffraction scan, five parameters were used to fit the data: (1) an overall

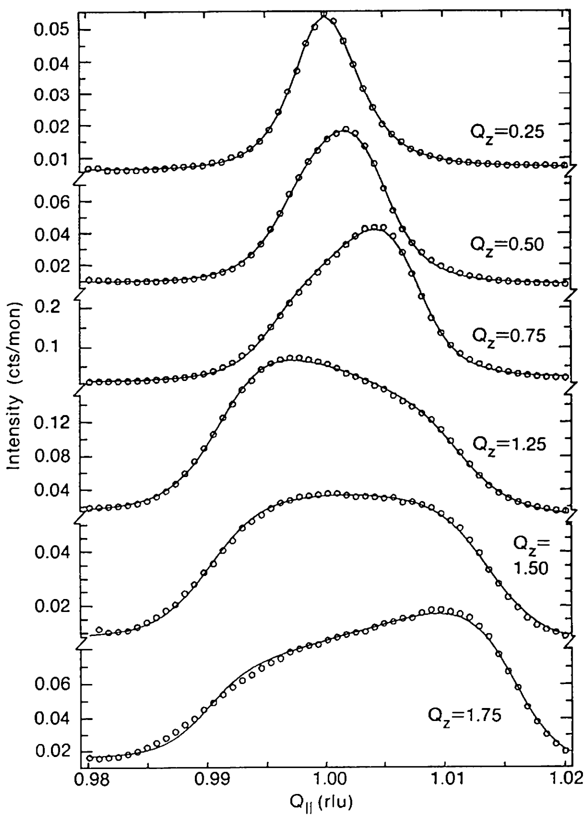

Fig. 5. $Q_\parallel$ scans of a CTR from an Ag(111) surface at different Q_z. The solid lines show fits to the data using the integral expression for $I_m(\mathbf{Q})$ [(52)]. Since the silver substrates have both *ABC* and *CBA* stacking, there are contributions from the ($10Q_z$) and the ($01Q_z$) CTRs and bulk Bragg peaks occur at both $Q_z = 1$ and $Q_z = 2$ r.l.u.

scale factor; (2) the out-of-plane width $\Delta Q_p \sin\chi$; (3) the in-plane width b; (4) a constant background term; and (5) a linear background term. Considering the simplifications and approximations, the fits are excellent.

Fig. 6(a) shows the fitting parameter $\Delta Q_p \sin\chi$ as a function of $\sin\chi$. The filled circles are taken from the fits shown in Fig. 5 and the open triangles are from fits to data obtained on the same Ag(111) substrate but with a thallium monolayer adsorbed on the surface. Since the monolayer is modulated by the substrate, $F_{hk}(Q_z)$ is modified from (51) (Toney *et al.*, 1990), but this change is small and we can neglect it here. The solid line in Fig. 6(a) shows a linear least-squares fit to the data that is constrained to pass through the origin. The observed linearity validates the approach we have taken to describe the $Q_\parallel$ line shapes. From the slope of this line, we determine the out-of-plane resolution as $\Delta Q_p = 0.048$ (1) r.l.u. or 0.121 (4) Å^{-1}. This is as expected for our experimental arrangement, where slits defined the out-of-plane collimation to be 24 mrad (*e.g.* $\Delta Q_p = (2\pi/\lambda)0.024 = 0.122\ \text{Å}^{-1}$).

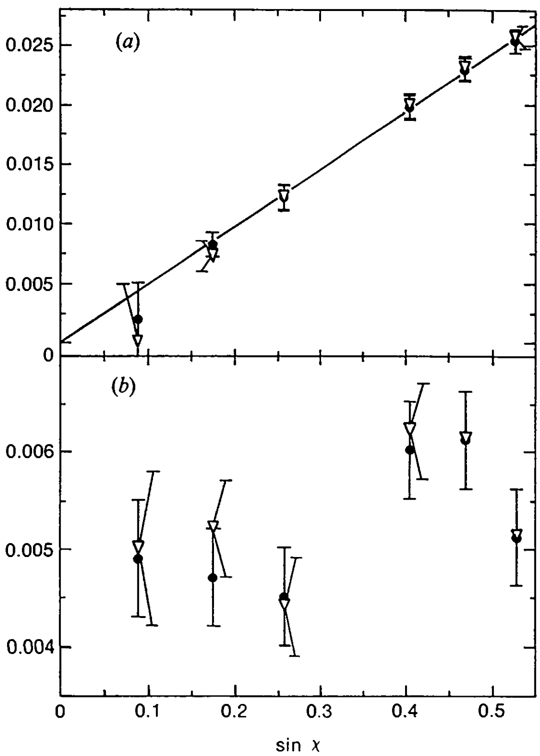

Fig. 6. The dependence of the fitting parameters $\Delta Q_p \sin\chi$ and b on $\sin\chi$. The filled circles are taken from the fits shown in Fig. 4 and the open triangles are from fits to data obtained on the same Ag(111) substrate but with a thallium monolayer adsorbed. (a) The out-of-plane width of the resolution function, $\Delta Q_p \sin\chi$. The solid line shows a linear least-squares fit through these data with the constraint that the line goes through the origin. (b) The Lorentzian-squared width b.

Fig. 6(b) shows the χ dependence of the Lorentzian-squared width b, which suggests there is a small but systematic dependence of b on χ. As discussed in Appendix D, this small dependence is expected and results from neglecting the $\cos\chi$ dependence in the expression for $H(Q_x, q_p, \chi)$ [*i.e.* using $H(Q_x, q_p, \chi) \simeq G(Q_x - q_p \sin\chi - G_{hk})$]. Because this approximation is best for small χ, we use the values of b for the two smallest χ to obtain $b = 0.0050$ (3) r.l.u. or 0.012 (1) Å^{-1}. From this and $\Delta Q_{st} \simeq 0.005\ \text{Å}^{-1}$, we estimate the intrinsic silver FWHM as $w_0 \simeq 0.015\ \text{Å}^{-1}$, assuming the FWHMs add in quadrature.

C. Resolution correction for Q_z scans

In § III.C, we found that the resolution correction for Q_z scans along a CTR was given by $\mathcal{R}_{pk}(\chi) = J(G_{hk}, \chi)$ [(22)]. For our Ag(111) data, the in-plane line shape is well described by a Lorentzian squared and this leads to

$$\begin{aligned}\mathcal{R}_{pk}(\chi) &= (1/k \sin\chi) g[(\Delta Q_p \sin\chi)/2] \\ &= (G_{L2}/k \sin\chi)\{[tb/(t^2+b^2)] \\ &\quad + \tan^{-1}(t/b)\}_{t=(\Delta Q_p \sin\chi)/2}. \end{aligned} \tag{53}$$

The solid line in Fig. 7 shows $\mathcal{R}_{pk}(\chi)$ using the values of ΔQ_p and b obtained from fits to the $Q_\parallel$ scans described above. We have set $G_{L2} = 2k/\pi$ so that $\mathcal{R}_{pk} \simeq 1/\sin\chi$ for large χ. It is of interest to compare this result for a squared Lorentzian with $\mathcal{R}_{pk}$ for a Gaussian line shape. For the latter, (18) shows

$$\begin{aligned}\mathcal{R}_{pk}(\chi) &= [(2\pi)^{1/2} G_G/k \sin\chi] \\ &\quad \times \operatorname{erf}(\Delta Q_p \sin\chi / 2^{3/2}\sigma_G). \end{aligned} \tag{54}$$

This is illustrated by the dashed line in Fig. 7, where we have used the same values of ΔQ_p and the in-plane FWHM as used for the Lorentzian squared and where we have taken $G_G = k/(2\pi)^{1/2}$ so that again $\mathcal{R}_{pk} \simeq 1/\sin\chi$ for large χ. A comparison of the solid and dashed curves shows that, for $Q_z > 1\ \text{Å}^{-1}$, they are in good agreement but, for $Q_z < \text{Å}^{-1}$, there are differences of order 10%.

D. Active sample area

Here we show the active area for the Gaussian beam used in our experiments on Ag(111) and compare this with the rectangular-beam approximation. For simplicity, we neglect the X-ray absorption factor $\exp(-2\mu T/\sin\alpha)$. Fig. 8 shows the dependence of $\mathcal{A}$ on Q_z calculated from (50) for our experimental conditions. As expected, the area is large for small Q_z and decreases as Q_z increases, falling off as $1/\sin\alpha$ for $Q_z \gtrsim 1.5\ \text{Å}^{-1}$. The dashed lines show $\mathcal{A}$ for a rectangular beam as obtained in § V.A: $\mathcal{A} = [(2\pi)^{1/2}\sigma_2 L_s]/(\sin^2\theta + \cos^2\chi \cos^2\theta)^{1/2}$ for small Q_z

and $\mathscr{A} = 2\pi\sigma_1\sigma_2/\sin\alpha$ for large Q_z, where we have used $F_i = (2\pi)^{1/2}\sigma_i$, $i = 1, 2$ (see § V.*B*). Fig. 8 illustrates that these expressions are valid only for $Q_z \lesssim 0.25$ Å^{-1} and $Q_z \gtrsim 1.5$ Å^{-1}, respectively. Between these values, where most of our data lie, it is necessary to account for the smoothly varying shape of the incident beam and the more accurate expression (50) must be used.

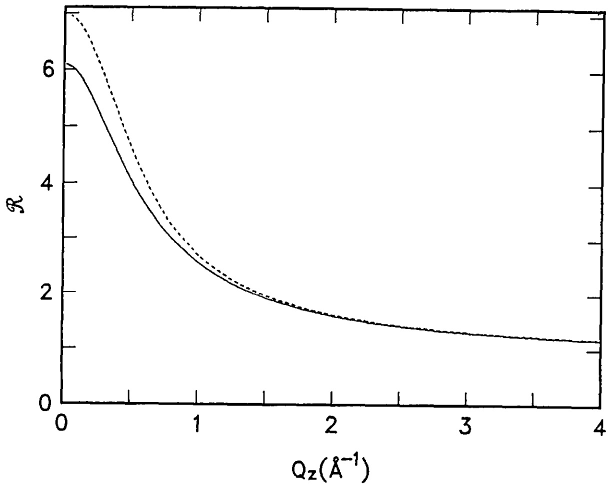

Fig. 7. Resolution correction $\mathscr{R}_{pk}$ for Lorentzian-squared [solid line, (53)] and Gaussian [dashed line, (54)] in-plane line shapes. For the Lorentzian-squared line shape, the widths of the resolution function and the surface diffraction peak are those obtained from the fits in Fig. 6: $\Delta Q_p = 0.048$ r.l.u. and $b = 0.0050$ r.l.u. For the Gaussian line shape, we have used the same ΔQ_p and a Gaussian r.m.s. width ($\sigma_G = 0.00273$ r.l.u.) such that the FWHM of the Lorentzian squared and the Gaussian are the same. In both calculations, the resolution function out of the scattering plane has a square-wave shape.

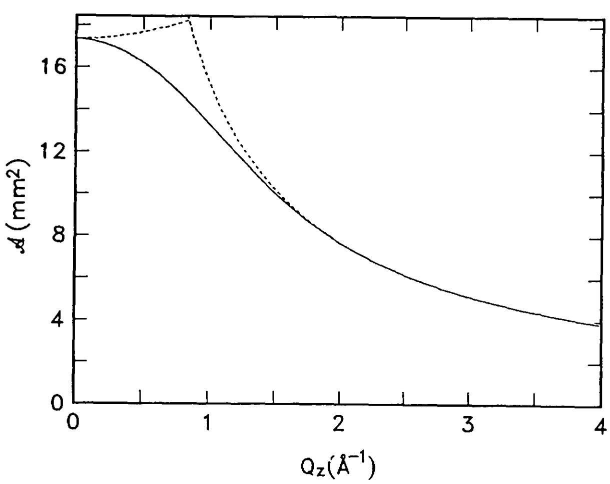

Fig. 8. Active sample area. The solid line shows $\mathscr{A}$ for a Gaussian shaped beam [(50)], while the dashed line shows $\mathscr{A}$ for a rectangular beam [(41) and (45)]. The incident-beam r.m.s. widths are $\sigma_2 = 0.33$ and $\sigma_1 = 0.73$ mm and the sample length is $2L_s = 21$ mm.

Table 3. *Principal results and relevant equation numbers and sections of this paper*

Result and description	Section and equation(s)
Measured intensity for low Q_z, permits determination of $G(t)$	§ III.*A*; (13)
Measured intensity at large Q_z, describes how the $Q_\parallel$ line shapes depend on Q_z	§ III.*B*; (18)
Q_z dependence of $Q_\parallel$ line shapes for in-plane line shapes [$G(t)$] that are Gaussian, Lorentzian and Lorentzian squared	§ III.*B*; (19) and Table 2
Measured peak intensity in Q_z scans or scans along a surface diffraction rod; relation to the rod structure factor; peak intensity resolution correction	§ III.*C*; (22)
Q_z dependence of the integrated peak intensity in φ and ω scans and relation to the rod structure factor; integrated intensity resolution correction	§ III.*E*; (27) and (28)
Integrated intensity resolution correction for a Gaussian in-plane line shape [$G(t)$]	§ IV; (33)
Active sample area for uniform rectangular distribution of the incident flux	§ V; (41), (43) and (45)
Active sample area for Gaussian distribution of the incident flux	§ V; (50)

VII. Summary and concluding remarks

In this paper, we have discussed how the instrument resolution affects measured intensities in surface X-ray scattering when Q_z is not small and when the symmetric four-circle geometry is employed. By assuming a square-wave shape for the resolution function out of the scattering plane, but an arbitrary in-plane shape, and by assuming that the surface scattering can be separated into functions of $Q_\parallel$ and Q_z, we have calculated the line shapes and intensities for a variety of scan directions. We have further calculated the resolution correction that is needed to convert rod intensities into structure factors and have treated both peak and integrated intensities. The locations within this paper of its principle results are shown in Table 3.

Our results are valid for nearly all Q_z and, most importantly, can be used for intermediate Q_z, where the resolution correction had not been well understood. Comparison of our results with previous treatments (Robinson, 1988; Altman, Estrup & Robinson, 1988; Gibbs, Ocko, Zehner & Mochrie, 1988; Ocko, Gibbs, Huang, Zehner & Mochrie, 1991; Sandy, Mochrie, Zehner, Huang & Gibbs, 1991) gives good agreement for large Q_z but shows differences for $Q_z \lesssim 0.5$–1 Å^{-1}. Support for our treatment is obtained from the excellent agreement between our expressions and data from an Ag(111) surface.

We also calculate the active sample area for an incident X-ray beam that is not spatially uniform, as is appropriate for experiments using focusing optics. Our expressions account for the active area more accurately than that for a uniform rectangular beam, particularly for $0.2 \lesssim Q_z \lesssim 1.5$ Å^{-1}. In our treatment of the active area, we introduced a generalized resolution function and discussed conditions where this decouples into the active area and the usual resolution function (dependent on only angular variables). We stress that these conditions are usually satisfied and this provides good justification for the general use of the usual resolution function.

By considering a more realistic resolution function and incident-beam shape, we have refined previous calculations of how these influence intensities and line shapes in measurements of surface diffraction rods (Robinson, 1988; Altman, Estrup & Robinson, 1988; Gibbs, Ocko, Zehner & Mochrie, 1988; Ocko, Gibbs, Huang, Zehner & Mochrie, 1991; Sandy, Mochrie, Zehner, Huang & Gibbs, 1991). The approach described in this paper quantitatively explains the line shapes for in-plane scans and enables more accurate determination of structure factors from measurements of surface diffraction rods for, essentially, all Q_z. Our approach is particularly significant for measurements at moderate values of Q_z ($\sim$0.2–1 Å^{-1}), which can be important in surface and interfacial systems (Samant, Brown & Gordon, 1991; Rabedeau, Toney, Harp, Farrow & Marks, 1992; Toney, Farrow, Marks, Harp & Rabedeau, 1992).

We thank Jean Jordan-Sweet and Brian Stephenson for their assistance with beam line X20*A*, Ian Robinson for lending us his Soller slits, and Gary Borges, Joe Gordon, Owen Melroy, Mahesh Samant, Larry Sorensen and Dennis Yee for assistance with the experiments on Ag(111). This work was performed at the National Synchrotron Light Source, Brookhaven National Laboratory, which is supported by the US Department of Energy, Division of Materials Science and Division of Chemical Sciences.

APPENDIX *A*
Coordinate systems

Here, we summarize equations related to our two coordinate systems. The first system is that of the sample and here $\hat{\mathbf{z}}$ is the surface normal and $\hat{\mathbf{x}}$ and $\hat{\mathbf{y}}$ are unit vectors parallel to the sample surface. The second coordinate system is defined by $\mathbf{Q}$ and the scattering plane; the unit vectors are $\hat{\mathbf{s}}$, $\hat{\mathbf{t}}$ and $\hat{\mathbf{p}}$, where $\hat{\mathbf{s}}$ is parallel to $\mathbf{Q}$, $\hat{\mathbf{t}}$ is perpendicular to $\mathbf{Q}$ but in the scattering plane and $\hat{\mathbf{p}}$ is perpendicular to the scattering plane. These are illustrated in Fig. 1. The connection between the coordinate systems is

$$\begin{aligned}\hat{\mathbf{s}} &= \cos\chi\cos\varphi\hat{\mathbf{x}} + \cos\chi\sin\varphi\hat{\mathbf{y}} + \sin\chi\hat{\mathbf{z}}\\ \hat{\mathbf{t}} &= -\sin\varphi\hat{\mathbf{x}} + \cos\varphi\hat{\mathbf{y}}\\ \hat{\mathbf{p}} &= -\sin\chi\cos\varphi\hat{\mathbf{x}} - \sin\chi\sin\varphi\hat{\mathbf{y}} + \cos\chi\hat{\mathbf{z}}.\end{aligned} \tag{55}$$

In the scattering-plane coordinate system, the average incident wavevector $\mathbf{k}_I$, average scattered wavevector $\mathbf{k}_F$ and scattering vector $\mathbf{Q} = \mathbf{k}_F - \mathbf{k}_I$ are (see Fig. 1)

$$\begin{aligned}\mathbf{k}_I &= -k\sin\theta\hat{\mathbf{s}} - k\cos\theta\hat{\mathbf{t}}\\ \mathbf{k}_F &= k\sin\theta\hat{\mathbf{s}} - k\cos\theta\hat{\mathbf{t}}\\ \mathbf{Q} &= 2k\sin\theta\hat{\mathbf{s}}.\end{aligned} \tag{56}$$

If we now consider $\varphi = 0$ (as we do in our derivation of $\mathscr{A}$), the equations above give

$$\begin{aligned}\mathbf{k}_I/k &= -\sin\theta\cos\chi\hat{\mathbf{x}} - \cos\theta\hat{\mathbf{y}} - \sin\theta\sin\chi\hat{\mathbf{z}}\\ \mathbf{k}_F/k &= \sin\theta\cos\chi\hat{\mathbf{x}} - \cos\theta\hat{\mathbf{y}} + \sin\theta\sin\chi\hat{\mathbf{z}}\\ \hat{\mathbf{p}} &= -\sin\chi\hat{\mathbf{x}} + \cos\chi\hat{\mathbf{z}}\\ (\mathbf{k}_I\times\hat{\mathbf{p}})/k &= \cos\theta\cos\chi\hat{\mathbf{x}} - \sin\theta\hat{\mathbf{y}} + \sin\chi\cos\theta\hat{\mathbf{z}}\\ (\mathbf{k}_F\times\hat{\mathbf{p}})/k &= -\cos\theta\cos\chi\hat{\mathbf{x}} - \sin\theta\hat{\mathbf{y}} - \sin\chi\cos\theta\hat{\mathbf{z}}.\end{aligned} \tag{57}$$

Armed with these expressions and noting that in the coordinate system of the sample, the position $\mathbf{r}$ is $\mathbf{r} = x\hat{\mathbf{x}} + y\hat{\mathbf{y}}$, we find

$$\begin{aligned}\mathbf{r}\cdot\hat{\mathbf{p}} &= -x\sin\chi\\ \mathbf{r}\cdot(\mathbf{k}_I\times\hat{\mathbf{p}}/k) &= x\cos\theta\cos\chi - y\sin\theta\\ \mathbf{r}\cdot(\mathbf{k}_F\times\hat{\mathbf{p}}/k) &= x\cos\theta\cos\chi + y\sin\theta.\end{aligned} \tag{58}$$

Now consider incident (scattered) X-rays that have angular deviations from the average direction of γ_i and β_i (γ_f and β_f) in and out of the scattering plane. The wavevectors of these X-rays are different from the average incident and scattered wavevectors ($\mathbf{k}_I$ and $\mathbf{k}_F$) and we have

$$\begin{aligned}\mathbf{k}_i &= -k\sin(\theta+\gamma_i)\cos\beta_i\hat{\mathbf{s}}\\ &\quad - k\cos(\theta+\gamma_i)\cos\beta_i\hat{\mathbf{t}} + k\sin\beta_i\hat{\mathbf{p}}\\ \mathbf{k}_f &= k\sin(\theta+\gamma_f)\cos\beta_f\hat{\mathbf{s}}\\ &\quad - k\cos(\theta+\gamma_f)\cos\beta_f\hat{\mathbf{t}} + k\sin\beta_f\hat{\mathbf{p}}.\end{aligned} \tag{59}$$

Keeping only linear terms (the angular deviations are small), we calculate $\mathbf{q}$, the deviation of the detected X-rays from $\mathbf{Q}$, as

$$\begin{aligned}\mathbf{q}(\gamma_i,\beta_i,\gamma_f,\beta_f) &\equiv \mathbf{k}_f - \mathbf{k}_i - \mathbf{Q} = q_s\hat{\mathbf{s}} + q_t\hat{\mathbf{t}} + q_p\hat{\mathbf{p}}\\ &= k(\cos\theta)(\gamma_f+\gamma_i)\hat{\mathbf{s}} + k(\sin\theta)\\ &\quad\times(\gamma_f-\gamma_i)\hat{\mathbf{t}} + k(\beta_f-\beta_i)\hat{\mathbf{p}}.\end{aligned} \tag{60}$$

This is inverted to yield

$$\begin{aligned}\gamma_i(q_s,q_t) &= (q_s/2k\cos\theta) - (q_t/2k\sin\theta)\\ \gamma_f(q_s,q_t) &= (q_s/2k\cos\theta) + (q_t/2k\sin\theta)\\ \beta_i(\xi,q_p) &= -(q_p/2k) + (\xi/2)\\ \beta_f(\xi,q_p) &= (q_p/2k) + (\xi/2),\end{aligned} \tag{61}$$

where $\xi = \beta_i + \beta_f$. To write $\mathbf{q}$ in sample coordinates, the transformation (55) is used, with the result

$$\begin{aligned}\mathbf{q} &= (q_s\cos\varphi\cos\chi - q_t\sin\varphi - q_p\cos\varphi\sin\chi)\hat{\mathbf{x}}\\ &\quad + (q_s\sin\varphi\cos\chi + q_t\cos\varphi - q_p\sin\varphi\sin\chi)\hat{\mathbf{y}}\\ &\quad + (q_s\sin\chi + q_p\cos\chi)\hat{\mathbf{z}}.\end{aligned} \tag{62}$$

APPENDIX B
Generalized instrument resolution function

Here, we derive a general form for the resolution function when the incident beam is monochromatic but imperfectly collimated and spatially inhomogeneous. The spatial flux density $\Phi(\mathbf{r})$ at $\mathbf{r}$ on the sample (measured in photons s^{-1} cm^{-2}) is

$$\Phi(\mathbf{r}) = \int d\gamma_i \, d\beta_i (\partial^2\Phi/\partial\gamma_i\partial\beta_i)(\gamma_i, \beta_i, \mathbf{r}), \quad (63)$$

where $\partial^2\Phi/\partial\gamma_i\partial\beta_i(\gamma_i, \beta_i, \mathbf{r})$ is the distribution function of X-rays deviating from the average incidence direction by angles γ_i and β_i in and out of the scattering plane, respectively. Note that $\partial^2\Phi/\partial\gamma_i\partial\beta_i(\gamma_i, \beta_i, \mathbf{r})$ is the spectral brilliance multiplied by the bandpass of the monochromator (an invariant) evaluated at the sample surface. We also define $\Delta(\gamma_f, \beta_f, \mathbf{r})$ as the probability of detecting an X-ray scattered at $\mathbf{r}$, where γ_f and β_f are the angular deviations from the average scattering direction in and out of the scattering plane, respectively. The detector count rate is determined by integrating over all possible paths of the incident and detected X-rays:

$$\begin{aligned} I_m(\mathbf{Q}) = \int & d\gamma_i \, d\beta_i \, d\beta_f \, d\gamma_f \, d^2r \\ & \times (\partial^2\Phi/\partial\gamma_i\partial\beta_i)(\gamma_i, \beta_i, \mathbf{r})\Delta(\gamma_f, \beta_f, \mathbf{r}) \\ & \times (d^2\sigma/d\Omega \, dA)[\mathbf{Q}+\mathbf{q}(\gamma_i, \beta_i, \gamma_f, \beta_f); \mathbf{r}], \end{aligned} \quad (64)$$

where $d^2\sigma/d\Omega \, dA$ is the differential X-ray scattering cross section per unit area on the surface and is an intrinsic function of the sample. The vector $\mathbf{q}$ is the deviation of the detected X-rays from $\mathbf{Q}$ (see Appendix *A*).

If the sample is spatially homogenous [condition (i)], the spatial and momentum components of $d^2\sigma/d\Omega \, dA$ decouple:

$$\begin{aligned} & (d^2\sigma/d\Omega \, dA)[\mathbf{Q}+\mathbf{q}(\gamma_i, \beta_i, \gamma_f, \beta_f); \mathbf{r}] \\ & = M(\mathbf{r}) \frac{d^2\sigma}{d\Omega \, dA}[\mathbf{Q}+\mathbf{q}(\gamma_i, \beta_i, \gamma_f, \beta_f)], \end{aligned} \quad (65)$$

where $M(\mathbf{r})$ is a shape function defined to be 1 at the sample surface and 0 elsewhere. Changing variables to $\xi = \beta_i + \beta_f$ and $\mathbf{q} = q_s\hat{\mathbf{s}} + q_t\hat{\mathbf{t}} + q_p\hat{\mathbf{p}}$, we define the generalized resolution function as

$$\begin{aligned} R(\mathbf{q}) = (1/2k^3 \sin 2\theta) \int & d\xi \, d^2r \\ & \times (\partial^2\Phi/\partial\gamma_i\partial\beta_i)[\gamma_i(q_s, q_t); \beta_i(\xi, q_p); \mathbf{r}] \\ & \times M(\mathbf{r})\Delta[\gamma_f(q_s, q_t); \beta_f(\xi, q_p); \mathbf{r}], \end{aligned} \quad (66)$$

where the expressions for $\gamma_i(q_s, q_t)$, $\beta_i(\xi, q_p)$, $\gamma_f(q_s, q_t)$ and $\beta_f(\xi, q_p)$ are given in Appendix *A*. With this definition, the measured intensity is

$$I_m(\mathbf{Q}) = \int d^3q \, R(\mathbf{q})(d^2\sigma/d\Omega \, dA)(\mathbf{Q}+\mathbf{q}). \quad (67)$$

As usual, this is the convolution of the (generalized) resolution function with the X-ray scattering from the sample.

Considerable simplification of $R(\mathbf{q})$ arises when one can separate both $\partial^2\Phi/\partial\gamma_i\partial\beta_i(\gamma_i, \beta_i, \mathbf{r})$ and $\Delta(\gamma_f, \beta_f, \mathbf{r})$ into spatial and angular functions. In most experimental arrangements, the detection probability involves little coupling between the position the X-ray scatters from ($\mathbf{r}$) and the direction it scatters into (γ_f, β_f). Thus, under this condition [(ii)], $\Delta(\gamma_f, \beta_f, \mathbf{r})$ can be separated:

$$\Delta(\gamma_f, \beta_f, \mathbf{r}) = \mathscr{D}(\gamma_f, \beta_f)\mathscr{D}'(\mathbf{r}). \quad (68)$$

Separation of $\partial^2\Phi/\partial\gamma_i\partial\beta_i(\gamma_i, \beta_i, \mathbf{r})$ into spatial and angular functions is more troublesome, since it is an invariant and Liouville's theorem applies. Thus, separation is not strictly possible unless the incident beam has zero divergence. (In other words, conservation of flux requires that the flux gradient is perpendicular to the local beam direction; if the beam is divergent, this causes the spatial profile of the beam to change as it propagates.) Despite this, separation of $\partial^2\Phi/\partial\gamma_i\partial\beta_i(\gamma_i, \beta_i, \mathbf{r})$ is a good approximation when two additional conditions are met: (iii) the beam is sufficiently collimated that its spatial profile does not change appreciably over the sample area; and (iv) the divergence of the incident beam is independent of position at the sample. Since these are usually satisfied, we use the approximation of separability and

$$(\partial^2\Phi/\partial\gamma_i\partial\beta_i)(\gamma_i, \beta_i, \mathbf{r}) = \mathscr{F}(\gamma_i, \beta_i)\mathscr{F}'(\mathbf{r}). \quad (69)$$

Combining (66)–(69), we obtain a simplified expression for the generalized resolution function:

$$R(\mathbf{q}) = \mathscr{R}(\mathbf{q})\mathscr{A}(\mathbf{Q}), \quad (70)$$

where

$$\begin{aligned} \mathscr{R}(\mathbf{q}) = (1/2k^3 \sin 2\theta) \int & d\xi \, \mathscr{F}[\gamma_i(q_s, q_t), \beta_i(\xi, q_p)] \\ & \times \mathscr{D}[\gamma_f(q_s, q_t), \beta_f(\xi, q_p)] \end{aligned} \quad (71)$$

is the usual resolution function (*e.g.* for a spatially uniform incident beam) and

$$\mathscr{A}(\mathbf{Q}) = \int d^2r \mathscr{F}'(\mathbf{r})M(\mathbf{r})\mathscr{D}'(\mathbf{r}) \quad (72)$$

is the active sample area. This is the sample area that is illuminated by the incident beam and viewed by the detector and it includes the X-ray absorption of the incident and scattered beams, since these are incorporated into $\mathscr{F}'(\mathbf{r})$ and $\mathscr{D}'(\mathbf{r})$.

References

ALTMAN, M., ESTRUP, P. & ROBINSON, I. (1988). *Phys. Rev. B*, **38**, 5211–5214.
BUSING, W. & LEVY, H. (1967). *Acta Cryst.* **22**, 457–464.

COOPER, M. & NATHANS, R. (1967). *Acta Cryst.* **23**, 357-367.
COWLEY, R. (1987). *Acta Cryst.* **A43**, 825-836.
FEIDENHANS'L, R. (1989). *Surf. Sci. Rep.* **10**, 105-188.
FEIDENHANS'L, R., PEDERSEN, J., NIELSEN, M., GREY, F. & JOHNSON, R. (1986). *Surf. Sci.* **178**, 927-933.
GIBBS, D., OCKO, B., ZEHNER, D. M. & MOCHRIE, S. (1988). *Phys. Rev. B*, **38**, 7303-7310.
KASHIHARA, Y., KIMURA, S. & HARADA, J. (1989). *Surf. Sci.* **214**, 477-492.
LUCAS, C., GARTSTEIN, E. & COWLEY, R. (1989). *Acta Cryst.* **A45**, 416-422.
LUCAS, C., HATTON, P., BATES, S., RYAN, T., MILES, S. & TANNER, B. (1988). *J. Appl. Phys.* **63**, 1936-1941.
MARRA, W., EISENBERGER, P. & CHO, A. (1979). *J. Appl. Phys.* **50**, 6927-6933.
OCKO, B., GIBBS, D., HUANG, K., ZEHNER, D. & MOCHRIE, S. (1991). *Phys. Rev. B*, **44**, 6429-6443.
PYNN, R., FUJII, Y. & SHIRANE, G. (1983). *Acta Cryst.* **A39**, 38-46.
RABEDEAU, T., TONEY, M., HARP, G., FARROW, R. & MARKS, R. (1992). Unpublished.
ROBINSON, I. (1986). *Phys. Rev. B*, **33**, 3830-3836.
ROBINSON, I. (1988). *Aust. J. Phys.* **41**, 359-367.
ROBINSON, I. (1989). *Rev. Sci. Instrum.* **60**, 1541-1544.
ROBINSON, I. (1991). In *Handbook on Synchrotron Radiation*, Vol. 3, edited by G. S. BROWN & D. E. MONCTON, pp. 221-266. Amsterdam: North Holland.
SAMANT, M., BROWN, C. & GORDON, J. (1991). *Langmuir*, **7**, 437-439.
SAMANT, M., TONEY, M., BORGES, G., BLUM, L. & MELROY, O. (1988*a*). *Surf. Sci.* **193**, L29-L36.
SAMANT, M., TONEY, M., BORGES, G., BLUM, L. & MELROY, O. (1988*b*). *J. Phys. Chem.* **92**, 220-225.
SANDY, A., MOCHRIE, S., ZEHNER, D., HUANG, K. & GIBBS, D. (1991). *Phys. Rev. B*, **43**, 4667-4687.
TONEY, M., FARROW, R., MARKS, R., HARP, G. & RABEDEAU, T. (1992). *Proc. Mater. Res. Soc.* **263-F2**, 273-280.
TONEY, M., GORDON, J., KAU, L., BORGES, G., MELROY, O., SAMANT, M., WIESLER, D., YEE, D. & SORENSEN, L. (1990). *Phys. Rev. B*, **42**, 5594-5603.
TONEY, M., GORDON, J., SAMANT, M., BORGES, G., MELROY, O., YEE, D. & SORENSEN, L. (1992). *Phys. Rev. B*, **45**, 9362-9374.
TONEY, M. & MELROY, O. (1991). In *Electrochemical Interfaces: Modern Techniques for In-Situ Interface Characterization*, edited by H. D. ABRUNA, pp. 57-129. Berlin: VCH Verlag Chemie.
WARREN, B. (1969). *X-ray Diffraction*. Reading, MA: Addison-Wesley.

Acta Cryst. (1993). A**49**, 642–648

The Correction of Geometrical Factors in the Analysis of X-ray Reflectivity

BY A. GIBAUD AND G. VIGNAUD

Laboratoire PEC UA no. 807 *CNRS, Université du Maine,* 72017 *Le Mans CEDEX, France*

AND S. K. SINHA

Exxon Research Laboratory, Annandale, NJ 08801, *USA*

(*Received* 10 *October* 1992; *accepted* 14 *December* 1992)

Abstract

X-ray reflectivity is a powerful technique to study electron density profiles in the direction normal to the surface of a flat sample. As usual in scattering experiments, where the phase information is lost, it is necessary to build a model that can be used to calculate the reflectivity for comparison with the measured reflectivity. In the calculations, it is necessary to correct the calculated reflectivity from geometrical and resolution-function factors, which play a major role at low angles of incidence. These factors are presented in this paper and the corrected calculated intensity is compared with the measured reflectivity of a commercial silicon wafer and of a niobium film on a sapphire substrate.

1. Introduction

X-ray reflectivity is now widely used to determine the structure and the composition of flat surfaces in the direction normal to the sample face. The object of the reflectivity measurement is to determine the depth profile of electron density inside the material. The technique is highly appropriate to investigations of multilayers and polymer, magnetic and ferroelectric thin layers and also liquid surfaces (Russel, 1990; Als-Nielsen, 1984; Benatar, 1992). Such systems are of considerable scientific and industrial interest because their properties may differ considerably from those of the bulk materials, as is the case in magnetic ultrathin layers, and because periodic variation of the composition (as in multilayers) causes further differences in properties. In addition, the cost of thin layers is low compared with that of the bulk materials. Furthermore, thin layers are useful for insertion into integrated electronics, as, for example, with ferroelectric nonvolatile memories.

The measurement of X-ray reflectivity is in principle easy to carry out, especially for samples with large flat surfaces. However, even in this case, the finite size of the surface, combined with the non-

ISSN 0108-7673